

# 1 **Marine cloud base height retrieval from MODIS cloud properties using** 2 **machine learning**

3

4 Julien LENHARDT <sup>1</sup>, Johannes QUAAS <sup>1,2</sup>, Dino SEJDINOVIC <sup>3</sup>

5

6 <sup>1</sup>Leipzig Institute for Meteorology, Leipzig University, Leipzig, Germany

7 <sup>2</sup>ScaDS.AI - Center for Scalable Data Analytics and Artificial Intelligence, Leipzig University, Humboldtstraße 25, 04105

8 Leipzig, Germany

9 <sup>3</sup>School of Computer and Mathematical Sciences & Australian Institute for Machine Learning, University of Adelaide, Adelaide,

10 Australia

11 *Correspondence to:* Julien LENHARDT (julien.lenhardt@uni-leipzig.de)

## 12 Abstract

13

14 Clouds are a crucial regulator in the Earth's energy budget through their radiative properties, both at the top-of-the-atmosphere  
15 and at the surface, hence determining key factors like their vertical extent is of essential interest. While the cloud top height is  
16 commonly retrieved by satellites, the cloud base height is difficult to estimate from satellite remote sensing data. Here we present  
17 a novel method called **ORABase (Ordinal Regression Autoencoding of cloud Base)** leveraging spatially resolved cloud  
18 properties from the MODIS instrument to retrieve the cloud base height over marine areas. A machine learning model is built  
19 with two components to facilitate the cloud base height retrieval: the first component is an autoencoder designed to learn a  
20 representation of the data cubes of cloud properties and reduce their dimensionality. The second component is developed for  
21 predicting the cloud base using ground-based ceilometer observations from the lower dimensional encodings generated by the  
22 aforementioned autoencoder. The method is then evaluated based on a collection of co-located surface ceilometer observations  
23 and retrievals from the CALIOP satellite lidar. The statistical model performs well on both datasets, exhibiting accurate  
24 predictions in particular for lower cloud bases and a narrow distribution of the absolute error, namely 379 m and 328 m for the  
25 mean absolute error and the standard deviation of the absolute error respectively for cloud bases in the test set. Furthermore,  
26 cloud base height predictions are generated for an entire year over ocean, and global mean aggregates are also presented,  
27 providing insights about global cloud base height distribution and offering a valuable dataset for extensive studies requiring  
28 global cloud base height retrievals. The global cloud base height dataset and the presented models **constituting ORABase** are  
29 available from Zenodo (Lenhardt et al., 2024).

## 30 1 Introduction

31

32 Clouds play a key role in the Earth's energy budget through their interactions with incoming shortwave and outgoing longwave  
33 radiation fluxes. It is thus critical to adequately quantify cloud radiative properties and their changes under global climate  
34 change. However, cloud radiative properties remain a large uncertainty in estimating anthropogenic climate change and possible  
35 impacts in the future (Boucher et al., 2013; Forster et al. 2021). Radiative properties of clouds are related to numerous quantities  
36 that can be used to characterise them. For instance, the cloud base height (CBH) is a crucial radiative property through its impact  
37 on the surface longwave radiation. Furthermore, the cloud geometrical thickness (CGT), defined as the difference between the  
38 cloud top height (CTH) and the CBH, links to the adiabatic cloud water content allowing the quantification of the cloud's  
39 subadiabaticity. Additionally, deriving the CBH is of practical use for pilots, providing crucial information during flights.

40 However, while the CTH can be rather easily obtained through passive satellite observations, the CBH retrieval remains  
41 problematic due to the fact that it is only indirectly accessible to satellites, and due to retrieval errors related to satellite remote  
42 sensing such as instrument shortcomings or noisy measurements. Since the difference between the CTH and the CBH quantifies  
43 the vertical extent of a cloud, one way to retrieve the CBH from passive satellites is by making heavy assumptions on the vertical  
44 distribution of the cloud water path inside the cloud profile. It is thus a challenging retrieval with passive satellites data that  
45 provide information about the cloud top (e.g. cloud top temperature (CTT), pressure (CTP) or height (CTH)) or about the entire  
46 column (e.g. cloud optical thickness (COT)) assuming the cloud's adiabaticity. For example, Noh et al. (2017) rely on a  
47 semiempirical approach to link the CGT to the CTH and the cloud water path (CWP, includes both ice and liquid water paths). In  
48 a different approach, Böhm et al. (2019) retrieve the CBH from triangulation of a multi-angle spectroradiometer. However, in  
49 this case, assumptions were required on the distribution of convective clouds. On the other hand, active satellite remote sensing  
50 retrieves information with vertical resolution which greatly helps resolving the clouds vertical distribution. However, active  
51 satellite measurements can display attenuated signals close to the surface (Tanelli et al., 2008; Marchand et al., 2008) particularly  
52 in the presence of thick clouds or precipitation, rendering the retrieval of the CBH difficult even for radar and lidar. Among  
53 others, Mülmenstädt et al. (2018) and Lu et al. (2021) present methods focusing on low clouds which use the CBH from active  
54 satellite retrievals of neighbouring thin clouds as representative of the surrounding cloud field. Active remote sensing  
55 additionally suffers from the sparse sampling that is confined to a narrow swath below the satellite. Finally, Goren et al. (2018)  
56 combine information from both passive and active satellite remote sensing and rely upon an adiabatic cloud model to derive the  
57 CBH. ~~More generally, remote sensing retrievals of the CBH rely on the assumed homogeneity of the cloud field in the vicinity of  
58 its base.~~

59 The retrieval of the CBH using satellite remote sensing data relies on a number of simplifying assumptions and is, consequently,  
60 prone to errors. ~~Subsequently, uncertainties~~ ~~Subsequent uncertainties~~ in the estimation of the CBH ~~propagate into uncertainties~~  
61 ~~can then relate to uncertainties~~ in the overall cloud radiative effect (CRE) (Kato et al., 2011; Trenberth et al., 2009).

62 The method presented here ~~called~~ ORABase (Ordinal Regression Autoencoding of cloud Base) leverages passive satellite  
63 retrievals of cloud properties in combination with marine surface observations to derive the CBH of a cloud scene using a ~~an~~  
64 ~~innovative~~ machine learning (ML) model. The CBH retrieval method relies on level 2 satellite data, namely three different cloud  
65 properties which are CTH, COT and CWP. A convolutional neural network (CNN, LeCun et al., 1989; LeCun et al., 1995) model  
66 following the autoencoder (AE; Kramer, 1991; Hinton et al., 2006) framework is trained in a self supervised way to reconstruct  
67 the previously mentioned cloud properties. This type of artificial neural network has been widely used in computer vision  
68 (Krizhevsky et al., 2012; LeCun et al., 2010) but also more recently in various applications in climate science (Reichstein et al.,  
69 2019; Watson-Parris et al., 2022). Thereafter, an ordinal regression (OR; Winship et al., 1984) model is fitted to predict the CBH  
70 corresponding to the cloud properties, learning from ground-based marine CBH retrievals. These different steps constituting the  
71 method are summarised in [Figure 1](#) and detailed in section 2. The objective of the developed method is primarily to produce  
72 CBH retrievals with reduced uncertainty, and additionally to extrapolate CBH retrievals from local surface observations to a  
73 wider spatial and temporal coverage. Indeed, we hypothesise that the spatial pattern of the cloud field carries information about  
74 the CBH and that the CNN can exploit the potential non-linear relationship between the CBH and the satellite observations.  
75 Furthermore, as more accurate CBH retrievals are obtained from ground-based remote sensing observations which are only  
76 available at isolated locations, we capitalise on these retrievals to develop a satellite-based retrieval algorithm capable of  
77 generalising to global distributions. We sensibly reduce the scope of the study by focusing on lower clouds, in particular as  
78 ground-based CBH observations display higher accuracy compared to satellite-based retrievals in those cases, and as it is the  
79 lowest cloud which often matters most for e.g. the surface radiation budget. We also restrict the retrievals to marine regions to  
80 remove the impact of orography on surface observations especially for these same low level clouds. ~~Our developed ML model~~  
81 ~~aims to draw on the spatial information present in a cloud scene in combination with relevant cloud properties to inform the CBH~~

82 prediction. As the CBH is typically derived from the surface, we focus on lower clouds in particular as the retrieval quality is  
 83 generally higher for those clouds, and as it is the lowest cloud that often matters most (e.g. for the surface radiation budget). The  
 84 combination of satellite remote sensing and surface based CBH retrievals has the potential to provide robust global CBH  
 85 estimates.

86 Section 2 firstly introduces the datasets and the co-location between ground-based observations and satellite retrievals. Secondly,  
 87 the ML method constituting ORABase is described. In section 3 we evaluate our predictions against other methods including  
 88 Noh et al. (2017) and other products from active satellite measurements like the 2B-CLDCLASS-LIDAR product (Sassen et al.,  
 89 2008). Section 4 presents the global dataset of the CBH which is derived from the ML approach. We discuss the benefits and  
 90 remaining challenges of our method in section 5. Further details about the spatial distribution of the observations and the ML  
 91 method are included in the appendices A-E. Additional links to available data outputs and codes are listed in the corresponding  
 92 sections.

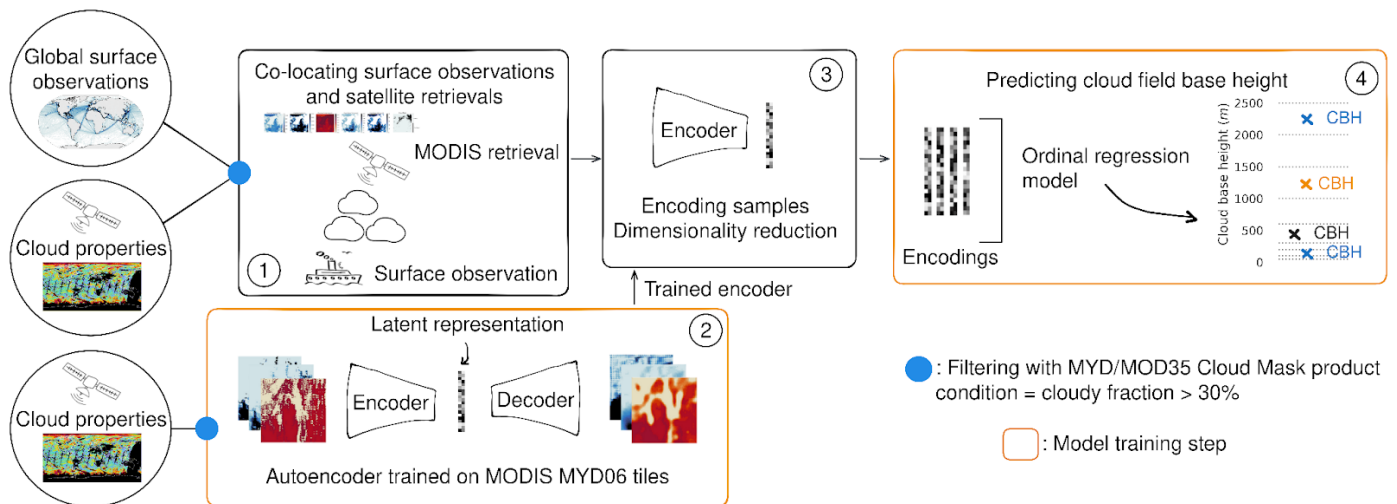
93

## 94 2 Data and methods

95

96 In this study we approach the retrieval of the CBH of a cloud scene by combining marine surface based observations of the CBH  
 97 and passive satellite retrievals of relevant cloud properties. The cloud scenes are defined within a tile of size 128 km x 128 km,  
 98 which incorporates different satellite retrieved cloud properties at a 1 km horizontal resolution from the MODerate Resolution  
 99 Imaging Spectroradiometer (MODIS, Platnick et al. (2017)). The satellite retrievals concern the CTH, the COT and the CWP,  
 100 which are related to the ground-based CBH observations (cf. Table 1). We focus on marine regions to remove the impact of  
 101 orography on surface observations especially for low level clouds. The approach is based on the assumption that the CBH is  
 102 homogeneous in the considered cloud scenes (similar to e.g., Böhm et al., 2019). To leverage the spatial extent of the cloud scene  
 103 and derive relevant features from the input channels, we rely on convolutional neural networks (CNNs, LeCun et al., 1989;  
 104 LeCun et al., 1995). This type of artificial neural network has been widely used in computer vision (Krizhevsky et al., 2012;  
 105 LeCun et al., 2010) but also more recently in various applications in climate science (Reichstein et al., 2019, Watson-Parris et al.,  
 106 2022). CNNs typically require a large number of labelled training samples due to their high number of parameters. However, the  
 107 co-location step between surface based observations and satellite retrievals limits the number of available data samples to train  
 108 the prediction model. We overcome this hurdle by introducing an unsupervised step using unlabeled satellite data. ¶

109 Hence, the novel method we present here can be summarised in four main steps (Fig. 1) and are further elaborated on in the  
 110 following sections: Firstly, we co-locate ground-based CBH observations and corresponding satellite-retrieved cloud properties  
 111 from MODIS (cf. sections 2.1, 2.2, 2.3 for more information on ground-based observations, satellite retrievals and co-location,  
 112 respectively). Secondly, we train an autoencoder (AE) with a CNN backbone solely on MODIS data in order to extract relevant  
 113 features from the cloud scenes (section 2.4). Thirdly, we project the cloud properties tiles from the co-located dataset to the latent  
 114 feature space constructed by the encoder. Ultimately, we predict the CBH from the encodings using an ordinal regression model  
 115 (section 2.5). ¶



116

117 **Figure 1: Schematic of the cloud base height retrieval method. 1) Co-location of surface-based cloud base height**  
 118 **observations and satellite retrievals. 2) Autoencoder training on satellite cloud properties. 3) Encoding of co-located**  
 119 **samples using the trained encoder. 4) Prediction of the cloud field base height.**

120

## 121 2.1 Surface observations

122

123 The CBH labels used in this study are part of a global marine meteorological observation dataset maintained by the UK Met  
124 Office (Met Office, 2006; [Table 1](#)), which provides observational data ongoing from 1854. The observations are conducted from  
125 measuring stations that were located on ships, buoys or platforms. As a consequence, this study largely relies on observational  
126 data representing the areas along the corresponding ship routes ([Fig. 2a](#)). ~~Despite their coarse resolution, the reported cloud base~~  
127 ~~observations provide valuable information about clouds in remote marine areas. The distribution of CBH observations and~~  
128 ~~corresponding bins are shown in [Figure 2](#).~~

129 At the beginning of meteorological and weather reports, surface-based cloud observations were retrieved manually or visually by  
130 human observers, but they have been gradually replaced by automated systems. ¶

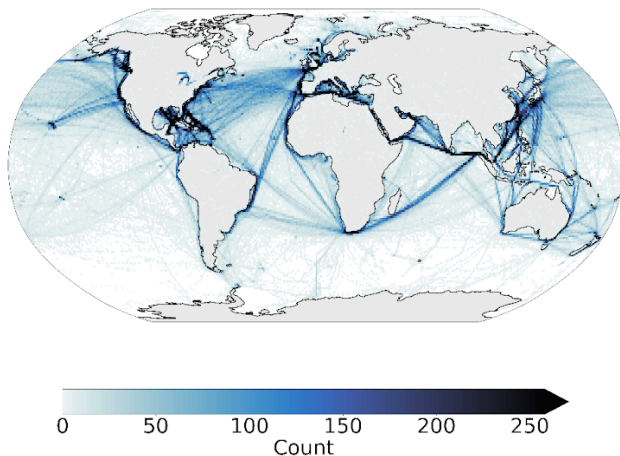
131 The CBH is derived using a ceilometer, an instrument based on a laser pointing upright and measuring the backscatter from the  
132 cloud base, and is then reported following the current standards from the World Meteorological Organisation (WMO; WMO,  
133 2019). The CBH observations are sorted into bins of increasing width (from 50 m to 500 m bin width) corresponding to the  
134 altitude ([Fig. 2b](#)) as the data transfer through radio limits the amount of transferable information and precision close to the  
135 surface is of importance notably for aircrafts. Since the actual measured CBH values are not available in the dataset, it is  
136 impossible to directly quantify a possible bias stemming from this binning process. In general here, we can suspect that the  
137 available CBH retrievals represent an accurate or underestimated assessment of the effective CBH, as for example a ceilometer  
138 measuring a CBH of 2490 m will be reported in the 2000 m bin in the available dataset. Using for example the central value of  
139 each bin could be another way to compute averages to potentially alleviate this unknown bias but it is not presented here.  
140 However, the method presented in the following sections predicts the CBH in corresponding bins, so it is left to the user to use  
141 these as they see fit for further analysis. ~~As a result, the binning process can lead to an underestimation of the actual CBH,~~  
142 ~~especially for a higher CBH for which the bin size is larger. In addition, the surface-based observations specify quantities like~~  
143 ~~temperature, humidity and wind speed at a given time and location.~~

144 ~~Despite their coarse resolution, the reported cloud base observations provide valuable information of clouds in remote marine~~  
145 ~~areas. The distribution of CBH observations and corresponding bins are shown in [Figure 2](#).~~

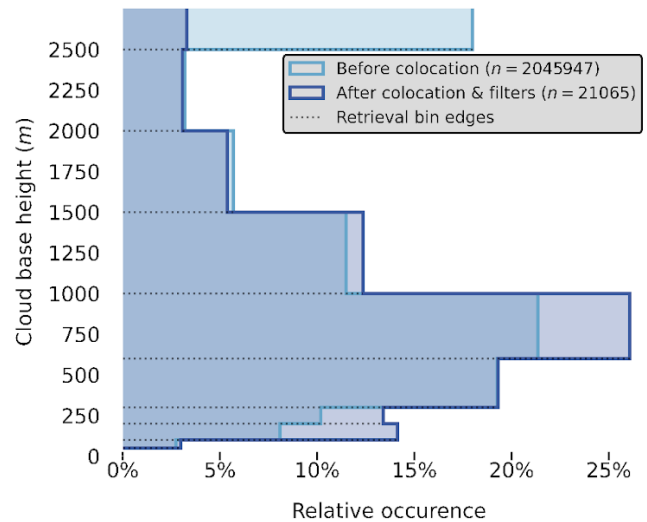
Data product	Description	Variables	Resolution	Usage
Global marine meteorological observations (Met Office, 2006)	Surface observations	Cloud base height (m)	Latitude/longitude coordinates 0.1° Hourly/daily observations	Labels
MODIS Atmosphere L2 Cloud Product (MYD06) (Platnick et al., 2017)	Cloud-top properties, cloud optical and microphysical properties	Cloud top height, CTH (m) Cloud optical thickness, COT (a.u.) Cloud water path, CWP (g.m <sup>-2</sup> )	1 km pixel resolution Daily overpass	Input features
MODIS Atmosphere L2 Cloud Mask Product (MYD35) (Ackerman et al., 2017)	Cloud pixel flag	Cloud mask	1 km pixel resolution Daily overpass	Used for cloud scene filtering

147 **Table 1 : Dataset description. The MODIS data are derived from the collection 6.1 of the datasets (Platnick et al., 2017;**  
 148 **Ackerman et al., 2017; cf. section 2.1). The surface observations are provided by a worldwide station network available**  
 149 **from the UK MetOffice (Met Office, 2006; cf. section 2.2).**  
 150

(a) **Cloud base height retrievals count**



(b) **Cloud base height retrievals distribution**



151

152

153 **Figure 2: (a) Spatial distribution of cloud base retrievals count (1° grid) and (b) distribution of the retrieved cloud base**  
 154 **height before and after the co-location and filtering process, for observations from the years 2008 and 2016.**

155

## 156 2.2 Satellite data

157

158 In this study we use products from the MODerate Resolution Imaging Spectroradiometer (MODIS, Platnick et al., 2017) MODIS  
 159 products from the AQUA satellites as input data that is later combined with the CBH labels derived from the surface-based  
 160 observations to train the prediction model. We choose MODIS satellite retrievals as they provide a large amount of data with  
 161 kilometre-scale resolution and daily overpasses, the. The spatial coverage of one granules with representing an area of is around  
 162 2330 km x 2000 km. We make use of the CUMULO dataset (Zantedeschi et al., 2019) since it provides already preprocessed  
 163 satellite data from the A-train with daily full coverage of the Earth for the years 2008 and 2016. In particular out of the available  
 164 variables we use two aligned products (cf. Table 1), namely the MODIS06 level 2 cloud product (hereafter MYD06; Platnick et

165 al., 2017) which provides relevant cloud properties and the MODIS35 level 2 cloud flag mask (hereafter MYD35; Ackerman et  
166 al., 2017) which allows us to filter scenes and screen for clouds.

167 The MYD06 product contains various cloud top properties (temperature, pressure, height) and cloud optical and microphysical  
168 properties (optical thickness, effective radius, water path). Level 2 data are derived from calibrated radiances through various  
169 algorithms and physical relations detailed in Platnick et al. (2017). The cloud top quantities are derived from radiance data of  
170 several channels. Wavelengths in the CO<sub>2</sub> absorption range are particularly used to identify the cloud top pressure (CTP) and thus  
171 the CTH of high clouds because of the opacity of CO<sub>2</sub>. For thicker or low boundary layer clouds, since the CO<sub>2</sub> slicing technique  
172 fails, ~~infrared bands (the CTH is retrieved using the 11 μm brightness temperature band are additionally required~~ and combined  
173 with simulated brightness temperatures based on vertical profiles from GDAS using surface temperature together with monthly  
174 averaged lapse rate data (Baum et al., 2012). The use of monthly averaged lapse rate data separately for different regions greatly  
175 helped reduce the bias in retrieved CTHs for low clouds in the Collection 6 of MYD06 from Collection 5, but some spatial and  
176 regional biases remain. These biases directly impact the spatial and temporal distribution of CTH in the data and thus what the  
177 model could learn from. The cloud optical thickness (COT) and cloud effective radius (CER) are simultaneously derived from  
178 multispectral reflectances, cloud masks, CTP data and surface type characteristics. The cloud water path (CWP) is additionally  
179 retrieved as part of the cloud optical properties algorithm described in Platnick et al. (2017). The retrieval of these cloud  
180 properties additionally requires inputs such as temperature, water vapour and ozone profiles from NCEP GDAS (Platnick et al.,  
181 2003; Baum et al., 2012) which can lead to potential uncertainties in particular in remote marine regions where only sparse  
182 observations are available for assimilation.

183 In general, the MYD06 level 2 product offers the advantage that the statistical model can be built relying on cloud properties and  
184 it can thus allow the study of relationships between the CBH and other cloud properties. Calibrated radiances, one step ahead in  
185 the data processing pipeline, would also provide insightful information but would require inputs of larger dimensionality since  
186 key information about clouds would be scarcer. Furthermore, using MYD06 level 2 data allows us to compare our method to  
187 others which in most cases use cloud properties to retrieve the CBH. ~~It is to be noted that~~ The level 2 product provides  
188 pre-processed data on top of the calibrated radiances and reflectances of level 1 data, which might introduce biases in the  
189 statistical model as previously mentioned regarding the CTH for example. From the entirety of available MYD06 retrievals, we  
190 select three cloud properties in particular, namely the CTH, COT, and CWP. The CTH is used as it provides key information  
191 about the CBH in the cloud field, as seen in Böhm et al. (2019). Vertically integrated cloud quantities like the COT and CWP  
192 further help the statistical model by providing key information about the cloud's vertical extent, lacking in cloud top only  
193 properties, making them commonly used for retrieving the CBH (e.g. Noh et al., 2017). The CWP as computed from COT and  
194 CER, and, in consequence, also the CBH are built on adiabatic assumptions (Grosvenor et al., 2018) and therefore cannot be used  
195 to constrain subadiabaticity as also highlighted in Mülmenstädt et al. (2018).

196

### 197 2.3 Datasets co-location

198

199 We proceed to ~~colocate~~ ~~match~~ our two data sources over the two years of MODIS MYD06 data available. To obtain the cloud  
200 properties of the cloud scene corresponding to the surface retrieval of CBH, we select a square tile of 128 km x 128 km from the  
201 closest MODIS ~~granuleswath~~ available centred around the observation location. Here *closest* means that the MODIS  
202 ~~granuleswath~~ contains the (latitude, longitude) coordinate of the CBH observation and the full extent of the tile centred around,  
203 and that the satellite retrieval was made during a one hour time-window before/after the CBH observation time. The spatial and  
204 temporal thresholds used to collocate the surface observations and the satellite retrievals are chosen for several reasons. Mainly,  
205 we want the satellite cloud properties to be representative of the cloud scene for which the CBH observation was made.  
206 Additionally, we want to recover a satisfying number of samples during the collocation process. Further arguments regarding the  
207 sensitivity of the retrieval method to the tile size are described in the following method section 2.5. ~~The spatial scale of the~~  
208 ~~extracted satellite retrieval was chosen in order to give enough spatial information to the AE while ensuring the measured CBH~~  
209 ~~is representative of the observed satellite retrieval. This spatial scale corresponds to using information from clouds in~~  
210 ~~approximately a 60 km radius around the observation location. Such a threshold is an adequate compromise between considering~~  
211 ~~all the relevant information while not discarding too many samples which might fall outside of the distance limit. These spatial~~  
212 ~~and temporal thresholds for the co-location are in line with other similar studies (Mülmenstädt et al. (2018) 100 km and 1 hour,~~  
213 ~~Lu et al. (2021) 150 km and 30 minutes; Böhm et al. (2019) 20 km and 15 minutes; Noh et al. (2017) 0.1 degree and 5 minutes)~~  
214 ~~even though the data products are partially different here. We furthermore add a condition that the corresponding tile is fully~~  
215 ~~located inside of the granuleswath to avoid any missing data in the cloud scene.~~

216 The extracted tile corresponding to the surface observation is then filtered. A first filter is applied to missing values in the  
 217 different cloud properties fields to primarily avoid retrievals of poor quality. This is predominantly the case for the COT and  
 218 CWP fields for which the retrieval fails more frequently, sometimes entirely. Another filtering is concordantly done using the  
 219 MYD35 product for cloud cover (minimum of 30% of cloudy pixels) to ensure the cloud field was substantial enough for the  
 220 colocated surface observation to be representative. Additional comments on the sensitivity of the CBH retrieval to this threshold  
 221 are presented in the following section on the downstream task of CBH prediction. Throughout the quality filtering process, the  
 222 missing data is one of the major factors impacting the amount of retained samples. On [Figure 2](#), we can see that it seems to  
 223 impact the clouds with higher CBHs. ~~is then filtered using the MOD35 product to only keep the cloud scenes with at least a 30%~~  
 224 ~~cloud cover. The latter condition is primarily aimed at retrievals of poor quality leading to missing pixels which is predominantly~~  
 225 ~~the case for the COT and CWP channels for which the retrieval fails more frequently. However it leads to a higher rate of~~  
 226 ~~removal for higher CBH observations ([Fig. 2](#)). Lowering the cloud cover filter led to a higher number of usable samples but~~  
 227 ~~ultimately did not improve the model's performance.~~

228 The overall filtering and co-location process yields around 21 000 samples. This only represents around 1% of the initial CBH  
 229 observations mainly due to the co-location process both in time and space with the MODIS overpasses. Missing values and cloud  
 230 cover filters are an additional factor in the reduced number of co-located samples. The presented co-located dataset is the basis to  
 231 build our cloud scene CBH retrieval prediction. ¶

232 ~~Classical semi-supervised pipelines, like the one presented here, characterised by a small labelled dataset and a vast unlabelled~~  
 233 ~~dataset, necessitate this kind of co-location or matching process. However, future avenues of research could consider directly~~  
 234 ~~modelling unmatched datasets, as in e.g. [Lun Chau et al. \(2021\)](#), which could additionally make use of other variables present in~~  
 235 ~~the surface observations.~~

236

## 237 2.4 Autoencoder

238

239 To circumvent the lack of labelled samples from which the relevant features are extracted, and to learn useful lower-dimensional  
 240 representations of the data, ~~work in a lower dimensional space,~~ we add a dimensionality reduction step to our method through an  
 241 unsupervised learning model. AEs ([Kramer, 1991](#); [Hinton et al., 2006](#)) offer a wide application spectrum, ranging from  
 242 preprocessing to the generation of new outputs. AEs are commonly used in unsupervised learning settings for reducing the  
 243 dimension of the input data to leverage the latent representations learned by the model to perform clustering, classification or  
 244 regression in a lower dimensional space ([Baldi et al., 2012](#)). We use classical AEs for their simplicity and versatility, but ~~it~~  
 245 ~~should be noted that~~ other approaches to unsupervised latent representation learning, such as variational AEs and its many  
 246 variants, can be used in a similar fashion. ¶

247 In general, AEs learn to encode the given input data to produce a latent representation of lower dimension. From the latent  
 248 representation, the input data is then reconstructed. The learning process is driven by what is called the reconstruction loss that  
 249 minimises the difference between the input and the reconstructed output.

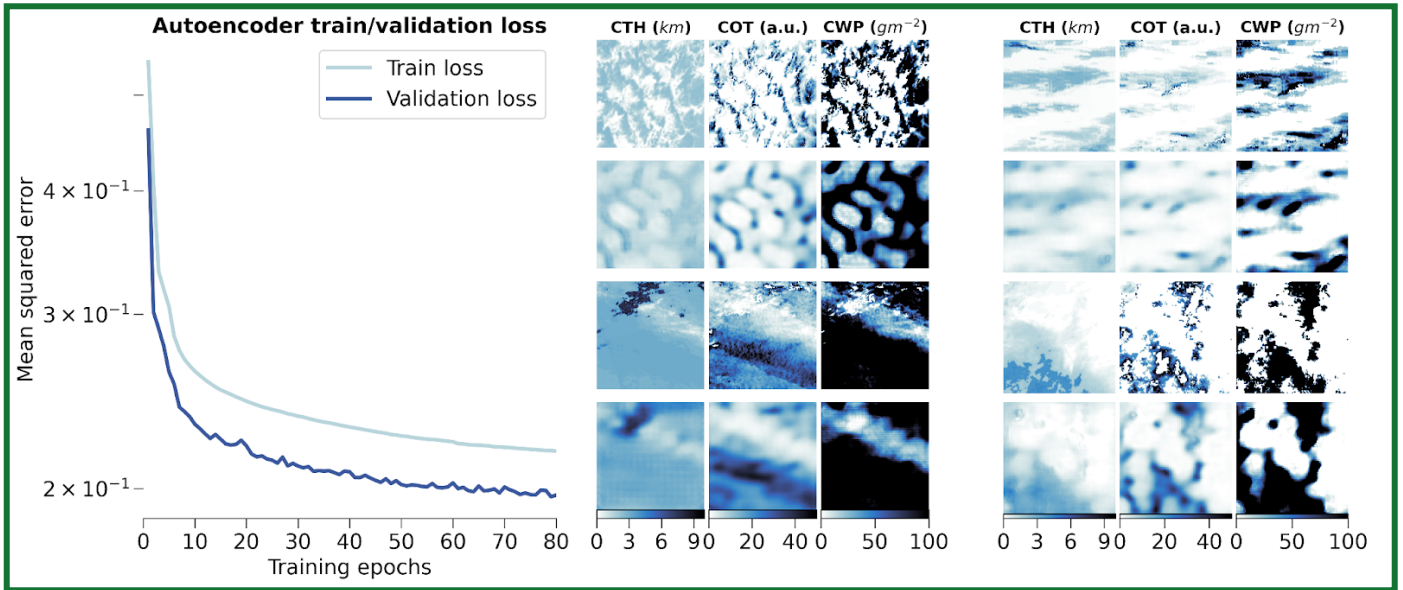
250 Here we use a convolutional AE architecture which is based on a CNN ([LeCun et al., 1989](#); [LeCun et al., 1995](#)) backbone in  
 251 order to leverage the spatial structure of our input data ([Pu et al., 2016](#)). In particular, we rely on the widely employed CNN  
 252 architectures U-Net ([Ronneberger et al., 2015](#)) and VGG ([Simonyan and Zisserman, 2015](#)), where the convolution layers are  
 253 based on 3x3 filters, stacked in blocks followed by maximum pooling layers, and mirrored for the decoder part of the model  
 254 using transposed convolution layers ([Zeiler et al., 2010](#)). We adapt the size of the input to fit our chosen tile size (128), the latent  
 255 space size to 256, and use the improved Leaky Rectified Linear Units (LeakyReLU; [Maas et al., 2013](#)) over the original ReLU  
 256 ([Nair and Hinton, 2010](#)) as activation functions. The detailed parameterization of the model is described in [Appendix B](#). The  
 257 model code was developed following implementations from the packages *PyTorch* ([Paszke et al., 2019](#)) and *TorchVision*  
 258 ([TorchVision, 2016](#)) and is included in the related Zenodo archive ([Lenhardt et al., 2024](#)). The main goal of the AE training is  
 259 then to minimise the loss function during the optimization or learning process, and to reproduce the input data with the highest  
 260 fidelity. For the loss function which in this case is only the reconstruction error, we use the common mean-squared error (MSE),  
 261 which can be written for a batch of samples as :

$$262 \quad \mathcal{L}_{reconstruction} = \frac{1}{N_i} \sum_{b \in B_i} \left\| b - D_{\theta}(E_{\theta}(b)) \right\|_2^2 \quad (1)$$

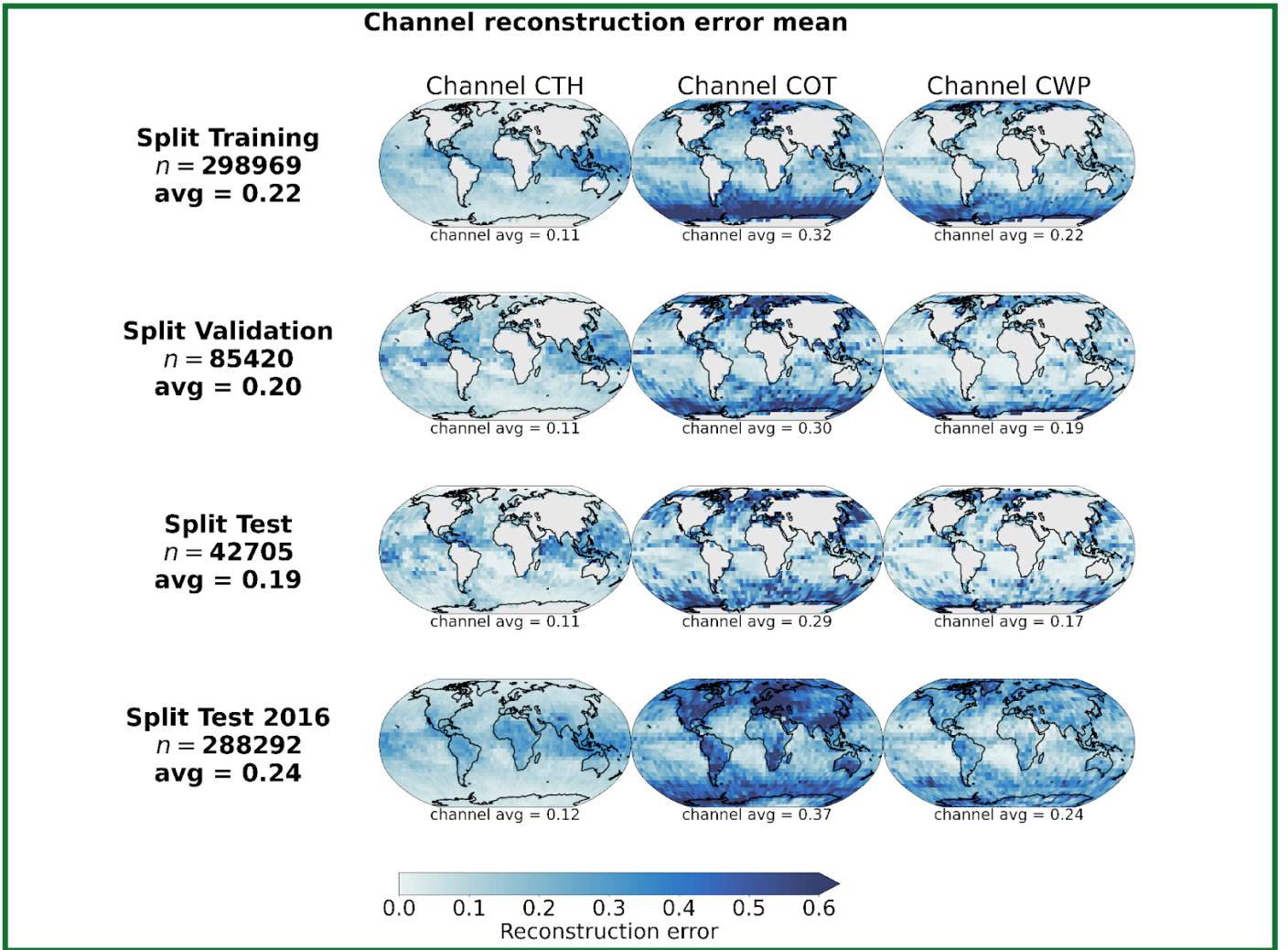
263 where, with the tiles used for training the AE noted as  $B = \{b_n \in \mathbb{R}^{3 \times 128 \times 128}\}_{n \in [1, N]}$ ,  $B_i$  represents a batch of samples of size  
 264  $N_i$  and  $\theta$  the combined parameters of the encoder  $E$  and decoder  $D$  models.



265 However, this self supervised step requires a large amount of data that the AE can learn from. Therefore, we select one full year  
 266 of data of MODIS granules from the CUMULO dataset (from the year 2008, cf. section 2.2) and randomly sample tiles following  
 267 the same criteria as during the co-location process (cf. section 2.3). We sample a maximum of 20 tiles from a single granule and  
 268 this for only a single year of data in order to avoid possible spatial and temporal auto-correlation in the data used for training and  
 269 testing leading to a non-representative performance of the mode (Kattenborn et al., 2022). Further details on the study of the  
 270 generalisation performance of the model for new observations in space and time are given in appendix B. The overall built  
 271 dataset consists of around 500 000 samples which are then splitted for training, validation and testing based on their retrieval  
 272 date. We additionally create a dataset based solely on data from the year 2016 for further testing which includes tiles not only  
 273 over ocean but also over land, indicating potential generalisation skill for unseen data including orography influence. The  
 274 reconstruction error during training and validation is shown in Figure 3 along with examples of reconstructed samples. The  
 275 spatially averaged reconstruction errors per cloud property channel are displayed in Figure 4 for each of the training, validation  
 276 and testing datasets previously mentioned. The trained model reaches an MSE of 0.19 on the test set and of 0.24 on the global  
 277 test set of 2016. The presented model is trained on tiles of size 128x128, but some arguments regarding the choice of the tile size  
 278 are made in the following section in the context of the downstream task of CBH prediction.



279 **Figure 3: (left) Training and validation losses during model optimization. (right) Examples of tiles (first and third rows)**  
 280 **with the corresponding reconstructions (second and fourth rows) for the different cloud property channels.**  
 281  
 282



283

284 **Figure 4: Spatial distribution of channel reconstruction errors aggregated on a 5° grid for the 2008 training, validation,**  
 285 **test and the 2016 test datasets.**

286 However, this unsupervised step requires a large amount of data that the AE can learn from. Therefore, we select one full year of  
 287 data of MODIS granuleswaths from the CUMULO dataset (from the year 2008, cf. section 2.2) and randomly sample tiles  
 288 following the same criteria as during the co-location process (cf. section 2.3). We thus create around 500 000 tiles to train our  
 289 model. We sample a maximum of 20 tiles from a single granuleswath and this for only a single year of data in order to avoid  
 290 possible spatial and temporal auto-correlation in the data used for training and testing leading to a non-representative  
 291 performance of the mode (Kattenborn et al., 2022). Further details on the study of the generalisation performance of the model  
 292 for new observations in space and time are given in appendix B.¶

293 Using the relevant MYD06 retrievals as input data (cf. section 2.2), we define several convolution layers grouped into a total of  
 294 five blocks for both the encoder and the decoder. The architecture of the decoder is thereby being mirrored to the encoder. Each  
 295 block consists of three convolutional layers with a kernel size of 3 and Leaky Rectified Linear Units (LeakyReLU; Maas et al.,  
 296 2013) as activation functions. At the end of each block, a maximum pooling layer is added with a kernel size and a stride of 2.  
 297 The model code was developed following implementations from the packages *PyTorch* (Paszke et al., 2019) and *TorchVision*  
 298 (TorchVision, 2016).¶

299 The main goal of the AE is to minimise the loss function during the optimization or learning process, and to reproduce the input  
 300 data with the highest fidelity. We denote the sampled tiles used for training the AE by  $B = \{b_i \in \mathbb{R}^{3 \times 128 \times 128}\}_{i \in [1, N]}$ , with

301  $N = 500\,000$ . A common choice for the reconstruction metric is the  $\ell_2$  norm:  $\mathcal{L}_{reconstruction} = \sum_{b \in B_i} \|b - D_{\theta}(E_{\theta}(b))\|_2^2$

302 where  $B_i$  represents a batch of samples and  $\theta$  the parameters of the encoder  $E$  and decoder  $D$  models. Details of the AE  
 303 architecture, training and performance are provided in appendix C.

304

## 305 2.5 Cloud base height ordinal regression

306

307 Once the AE’s optimization process is completed (cf. appendix C), the next step is to predict the corresponding CBH for the  
308 observed scene. As seen in Figure 2, the retrieved CBH observations are binned into different categories following WMO  
309 standards (WMO, 2019). This leads to a prediction problem at the intersection of regression (i.e. predicting numerical values)  
310 and classification (i.e. predicting the object class) called ordinal regression (OR; Winship et al., 1984). The labels from the target  
311 variable are defined by classes following a certain order, in this case the increasing CBH. A wide array of methods stems from  
312 this field with diverse applications for example in computer vision using neural networks (e.g. Niu et al., 2016; Shi et al., 2023;  
313 Lazaro and Figueiras-Vidal, 2023). Different methods exist to tackle such problem setups either via modification of the target  
314 variable, ordinal binary decomposition or threshold modelisation (Gutiérrez et al., 2016; Pedregosa et al., 2017). Threshold  
315 models were shown to be able to perform better than the ones designed for regression or multi-class classification on OR tasks  
316 (Rennie et al., 2005). We consider here two alternative frameworks in the case of threshold models which differ in how they  
317 penalise threshold violations: immediate-threshold (IT; Eq D.1) and all-threshold (AT; Eq D.2). The overall training process of  
318 the model aims at optimising a set of weights to project the input data to a one dimensional plane, subsequently dividing the  
319 constructed representation using learnable thresholds. These two implementations of threshold models are available from the  
320 *mord* Python package (based on Pedregosa, 2015) and further details on threshold OR models are added in appendix D.

321 To help evaluate the prediction model, we rely on a set of different metrics pertaining either to the regression aspect of the  
322 problem or to its classification/ordinal nature. First, the macro-averaged mean absolute error (MA-MAE) is used as it weights  
323 each class separately before averaging the subset MAEs, making it useful in the case of OR problems with imbalanced datasets  
324 (Bacianella et al., 2009). Using a macro-averaged metric prevents us from choosing a trivial model which might always predict  
325 the dominating class. Additionally, the macro-averaged root mean square error (MA-RMSE) is also used to investigate the skill  
326 of the prediction models. To assess the ordering of the predicted retrievals with respect to the labels, the ordinal classification  
327 index (OC; Cardoso and Sousa, 2011) and its updated version the uniform ordinal classification index (UOC; Silva et al., 2018)  
328 are computed. A version of the latter not requiring an extra hyperparameter, the area under the UOC (AUOC; Silva et al., 2018),  
329 is also reported. These different metrics are able to capture the proper ranking order of the predictions compared to the labels  
330 using the confusion matrix and also the overall accuracy of the prediction model. Nevertheless, one caveat is that these indexes  
331 developed for ordinal classification assume each class to be equally distant from another which is not the case here since the  
332 CBH retrievals are reported in bins of variable width. However, a purely ordinal classification index will drop all information on  
333 the scale of the response (1500 m misclassified as 600 m treated the same as 200 m misclassified as 50 m, since only the order  
334 matters) which might be not entirely appropriate for this problem. In an effort to address this limitation, the indexes are adapted  
335 to mimic the spacing between the different CBH bin classes by incorporating classes that are all spaced by 50 m, ranging from 50  
336 m up to 2500 m. In this manner, the CBH class difference is more suited to the actual nature of the retrieval. In particular, we  
337 use the OR implementation of threshold models from the *mord* Python package (based on Pedregosa, 2015). A  $\ell_2$  regularisation  
338 term is also added during the optimization process. We adopt the macro-averaged mean absolute error (MA-MAE) as our  
339 reference metric during hyperparameter tuning. This metric is in particular useful for OR problems when faced with imbalanced  
340 datasets (Bacianella et al., 2009). Using a macro-averaged metric prevents us from choosing a trivial model which might always  
341 predict the dominating class. We additionally reported the macro-averaged root mean square error (MA-RMSE) during training  
342 and validation of the models as it puts a larger penalty than the MAE on higher errors and is also a useful performance indicator.

343 However, several aspects of the ordinal regression model need to be investigated first. To this extent, we first divide our global  
344 colocated dataset (section 2.3) in training, validation and testing datasets but while ensuring each class is relatively equally  
345 represented in each split. The following aspects and sensitivities of the model to the input data parameters are assessed using the  
346 training and validation datasets: the potential benefit of using the spatial context through the AE, the input tile size and the cloud  
347 cover threshold. Moreover, the spatial generalisation skill of the model is studied by splitting the colocated dataset between the  
348 Northern and Southern hemispheres. For each of these, the performance for the AT variant of the OR model is reported as it  
349 performs significantly better than the IT variant across experiments and evaluation metrics.

350

### 351 2.5.1 Spatial context

352 In order to evaluate the actual effect of the spatial context with respect to the input cloud properties, the prediction skill of the  
353 model trained based on the AE encodings is compared to two trivial methods (predicting the majority bin and predicting the bin  
354 minimising the MAE across the training dataset) and a method relying on the flattened cloud properties of a 9x9 tile centred  
355 around the observation. Both of the trivial methods result in always predicting the CBH bin of 600 m. The third method yields a

356 similar dimensionality as the AE encodings (3 channels x 9 x 9 = 243) and thus helps to show how the AE potentially leverages  
357 some spatial information about the cloud scene. Across all metrics, the baseline method using the 9x9 tile input is outperformed  
358 by the initial method and even by the trivial choice of the majority bin, increasing the MA-RMSE by 400 m and the MA-MAE  
359 by 140 m compared to the OR predictions made with the AE. Using the trivial choice of the 600 m bin results in an increase of  
360 the MA-MAE (+7.7%) and of the MA-RMSE (+4.8%) compared to the base method. The mean bias of the trivial method is  
361 lowered closer to 0 m as it leads to a more substantial underestimation of the high CBHs and overestimation of the low CBHs. To  
362 conclude the comparison with these two other baselines, the information spatially encoded by the AE over the whole tile size  
363 area is useful in producing CBH retrievals of better quality compared to a baseline OR model with a reduced spatial context or a  
364 trivial method predicting a singular bin.

365

### 366 2.5.2 Tile size

367 A prediction model is fitted to the input data using encodings produced with tailored AE models trained as detailed in the  
368 previous section but with varying square input tile sizes of 16, 64 and 128. With the subsequent prediction models, the retrievals  
369 made with a tile size of 128 showcase the lowest MA-MAE (0.8% and 2.7% decreases compared to tile sizes of 16 and 64  
370 respectively) and MA-RMSE (around a 5% decrease compared to both other tile sizes), while no clear sensitivity arises from the  
371 OC, UOC or AUOC. Examining performance for each class separately indicates reduced errors (MAE and RMSE) for higher  
372 CBHs (above 1000 m) using the larger tile size of 128 and on par performance across tile sizes for lower CBHs. In the context of  
373 the presented CBH retrieval, the larger spatial information provided through the input tile seems to be useful for the subsequent  
374 CBH prediction task, leveraged with the help of the AE as shown previously.

375

### 376 2.5.3 Cloud cover

377 The colocated dataset is first filtered again with cloud cover thresholds of 10%, 20% and 30%. Each threshold respectively leads  
378 to datasets of 25 042, 23 034 and 21 065 samples which are then further splitted in training, validation and testing. On the  
379 validation set, while the decreases in MA-MAE (4.5%) and MA-RMSE (10%) with the 10% compared to the 30% cloud cover  
380 threshold are indicating a potential benefit of lowering the threshold, investigating the MAE and class-wise MAEs sheds a  
381 different picture: the benefit seems to marginally concern the higher CBH classes while hindering performances on low CBHs  
382 which overall explains the trend in RMSE notably. Considering the confusion matrices generated for each cloud cover threshold  
383 additionally shows that a lower cloud cover threshold results in a slightly increasing distribution shift of the predicted CBH  
384 classes towards higher CBHs, displaying a prediction cluster around 1000m. Overall, the benefit of additional available samples  
385 when lowering the cloud cover threshold does not seem to directly lead to convincing improved performance. The main axis of  
386 improvement here is probably lying in the widening of the collocation process to ensure broader spatial and temporal coverage of  
387 the training dataset.

388

### 389 2.5.4 Spatial generalisation

390 Furthermore, in a similar way as for investigating the spatial generalisation ability of the AE, we split our colocated dataset  
391 between the Northern and Southern hemispheres. This way, we ensure a minimal amount of samples in each spatial split (17 615  
392 and 3 450 for the Northern and Southern hemispheres respectively) even though the spatial distribution patterns of the retrievals  
393 greatly differ. As a result, the lower amount of samples in the Southern hemisphere leads to some overfitting with metrics  
394 systematically worsening when testing on the Northern hemisphere. However, the Northern hemisphere training displays fair  
395 generalisation skill with equal or improved metrics when testing on the Southern hemisphere, for example an 8% decrease in  
396 MA-RMSE, 1% decrease in OC and stable MA-MAE, UOC and AUOC. The class-wise performances for the two splits reveal  
397 the overall generalisation difficulty for higher CBHs (above 600 m) when training on the Southern hemisphere, as the labels  
398 relative to these classes are mostly present in the Northern hemisphere (Figure A.3). The ability of the model to generalise from  
399 the Northern hemisphere labels reassures the overall skill of the model once trained on all the labels available.

400

401 In the following section, we present the results of the developed method alongside comparisons to previous retrieval approaches.  
402 In particular, we compare our retrieval to a method assuming an adiabatic cloud model (adapted from Goren et al. (2018), cf.  
403 appendix E for implementation) and to the method from Noh et al. (2017). The former relies on the CTH retrieved from  
404 CALIPSO's Cloud Aerosol Lidar with Orthogonal Polarization (CALIOP; Hunt et al., 2009) and CloudSat (Stephens et al.,  
405 2008), but CWP and CTT retrievals from MODIS MYD06. However, in our own comparison study we used all necessary  
406 variables, including the CTH, from MODIS MYD06. The latter method relies on piecewise linear relationships between MODIS  
407 CWP and the geometric thickness of the uppermost layer from CALIPSO/CloudSat stratified by MODIS CTH. The application

of the method presented in Noh et al. (2017) is however done with CTH retrievals from the Suomi–National Polar-Orbiting Partnership (SNPP) VIIRS. The comparison to our method presented here is done by using the MODIS/CALIPSO/CloudSat-derived parameters from Noh et al. (2017), but using the MODIS derived CTH to produce the final CBH estimate. In both cases, since these methods can be applied pixel-wise when a MODIS retrieval is available, we computed the retrieved CBH values and averaged them over the cloud scene.

### 3 Results, evaluation, and comparison to previous retrieval approaches

414

#### 3.1 Cloud base height retrieval, evaluation and comparison to previous retrievals

416

In this section, we present the results of the retrieval, evaluate it using the ground-based observations, and investigate how our method fares by comparing it to a method assuming an adiabatic cloud model (adapted from Goren et al. (2018), cf. appendix E for implementation) and to the method from Noh et al. (2017). ~~It is to be mentioned that, for the former the sources of the CTH retrievals differ, and for the latter a different method was used for retrieving the CTH from the available MODIS CTP. For these two methods we first compute a CBH value for each cloudy pixel of the scene that is then averaged. The analysis is performed for the co-located scenes where ground-based observations are available. To be able to compare the relevant metrics for the different methods we proceed to a binning of the data following the WMO standard presented in section 2.1. In Table 2 we report several metrics including the MAE, the mean error (bias), the RMSE and the standard deviation of the absolute error. The latter helps us characterise the spread and uncertainty in the overall predictions with respect to the surface observations. We additionally report the adapted version of the AUOC mentioned in section 2.5. Furthermore, we do not report quantities such as the correlation coefficient or the regression line on the 2-dimensional histograms of Figure 35 and Figure 46, as the stratified and categorical aspects of the data would make reporting these not clearly informative. It is to be noted that later on we refer to the overall conceived method including the AE (cf. section 2.4) and the OR prediction model in the AT variant (cf. section 2.5), listed in Table 2 as ORABase. OR + AE, interchangeably as OR or as the prediction model.~~

We first note that the OR method with an immediate-threshold setup fails at predicting ~~with good accuracy~~ the cloud scene base height ~~with similar skill compared to the other retrieval products~~, producing large errors (double-fold in comparison to the all-threshold setup). On the other hand, ~~ORABase the OR method with an all-threshold setup~~ performs well with satisfying error measures and uncertainty in the predictions ~~on par with the other retrievals~~. Compared to the method from Noh et al. (2017), our method succeeds in decreasing on average the error, displaying a reduction of 100 m for the MAE. The method also effectively diminishes the uncertainty in the CBH retrievals, bringing down the absolute error standard deviation 200 m lower. Our method thus provides accurate retrievals with comparatively low general uncertainty levels. Even though on average the predictions exhibit a slight positive bias, we find that the CBH values above 2000 m are systematically underestimated (Fig. 35). In consideration of the low representation of such observations in the dataset, due to data filtering and surface observations being less reliable for higher clouds, the method still struggles to properly quantify the cloud scene base height of these samples. These samples also make up for most of the measurement uncertainty in the labels considering that ceilometers face challenges for retrieving cloud signals higher up in the boundary layer. Focusing on lower cloud scene base height retrievals, the predictions demonstrate even lower errors: the MAE is lowered to 379 m while the absolute error standard deviation is narrowed down to 328 m. Achieved accuracy levels and uncertainty measures attest to a certain trustworthiness of the cloud scene base height estimates, in particular in the context of product requirements for example the ones outlined by the Joint Polar Satellite System (JPSS; Goldberg et al. (2013); 2 km accuracy threshold). However, the cloud scene base height retrieval method presented here does not aim at constituting a product on its own as it is not operational with the processing of daily new data available from the MODIS instrument, but rather at providing robust estimates of CBH for lower level clouds. Therefore, it is expected and reasonable that the accuracies and uncertainties presented here are below such thresholds. However, the available method code (Lenhardt et al., 2024) easily allows the processing of new data for users, in addition to the available dataset for the year 2016.

We performed further sensitivity studies on our retrieval method trying to improve the quality of the predictions. An attempt to balance the dataset by oversampling the higher CBH values (cloud base retrievals falling into the 2500 m bin), however, did not yield better results overall but also posed a higher risk of overfitting to these specific samples. Furthermore, any spatial information about the location of the satellite retrieval was not included as to prevent possible overfitting to the latitude and longitude coordinates of the observations present in the training data. Since the observations are sparsely distributed especially in the southern hemisphere (cf. figures from appendix A), the goal is to avoid any kind of induced spatial bias and sensitivity in the model's predictions. Accordingly we can then ensure proper generalisation skill to new spatial areas, but not only based on known retrieval distributions at similar locations. ~~Correspondingly, the generalisation skill of the model requires further~~

assessment to guarantee meaningful and representative predictions. Spatial generalisation is rather challenging as the co-located samples are so sparsely distributed (Fig. A.3, Fig. A.4). Limiting the training dataset to a selected area would greatly hinder the representativeness notably because the different labels display diverse spatial patterns. As a consequence, the choice was made to evaluate the potential generalisation skill of the prediction model by establishing a geographic distribution of the mean predicted cloud scene base height for a whole year’s worth of MODIS overpasses. This is discussed in more detail in section 4. On the other hand, the temporal aspect of the model’s generalisation skill was intrinsically ensured by building a test set temporally distinct from the training set, including co-located samples only from the last months of 2016.

466

Method	MAE (m)	Bias (m)	RMSE (m)	Absolute error standard deviation (m)	AUOC
Goren et al. (2018)	457	- 262	689	515	0.92
Noh et al. (2017)	578	- 35	860	638	0.92
OR (IT) + AE	991	+ 595	1296	836	0.93
<b>ORABaseOR- (AT) + AE</b>	<b>447</b>	<b>+ 58</b>	<b>614</b>	<b>420</b>	<b>0.89</b>
ORABase training	456	+ 80	620	420	0.89

467

468 **Table 2: Performance on the test set of different CBH retrieval methods. OR models are either built with the immediate-**  
469 **threshold (IT) or all-threshold (AT) variant. The method on which the rest of the study is based has been highlighted in**  
470 **bold and its corresponding performance on the training set is added in the last row.**

471

### 472 3.2 Comparison to spaceborne radar-lidar retrievals of the CBH

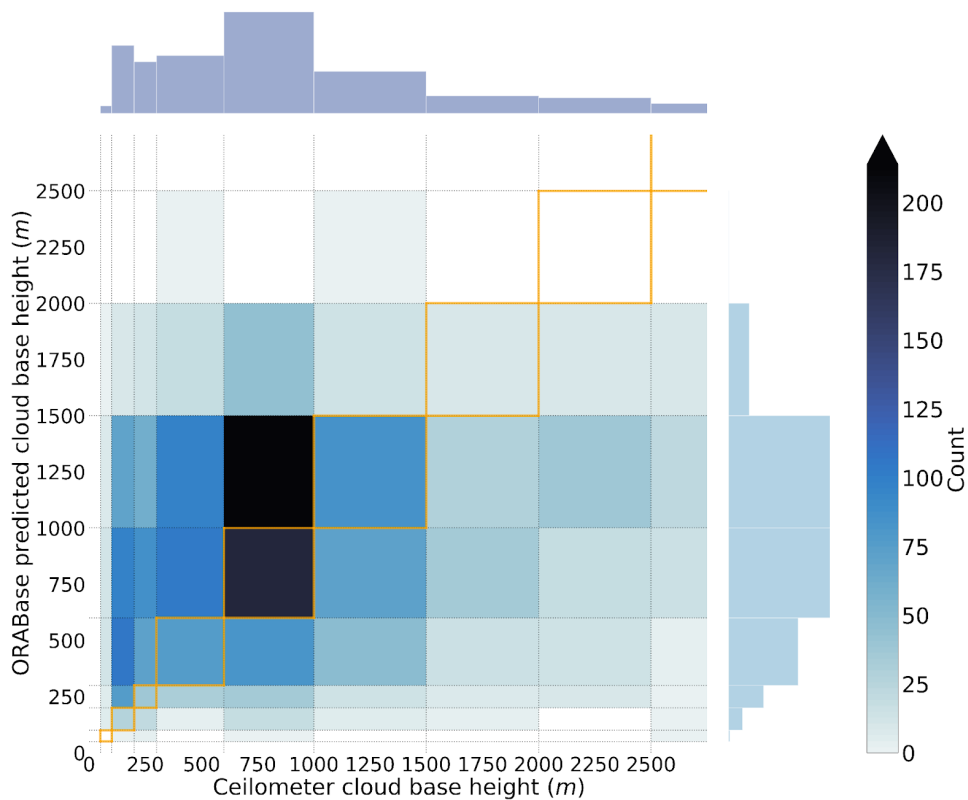
473

474 The combined datasets which are part of CUMULO (Zantedeschi et al., 2019), in particular the radar and lidar retrievals, facilitate the joint evaluation of our method with both ceilometer surface observations and active satellite retrievals. Specifically we leverage the 2B-CLDCLASS-LIDAR product (Sassen et al., 2008) which is derived from the combination of CloudSat’s Cloud Profiling Radar (CPR; Stephens et al., 2008) and CALIPSO’s Cloud-Aerosol Lidar with Orthogonal Polarisation (CALIOP; Hunt et al., 2009). The base height of the lowest cloud layer retrieved by the instruments in each scene is considered the scene CBH and then averaged over the available pixels along the track, preserving the same spatial extent as the associated cloud properties from the MODIS instrument. For the co-located samples of the year 2008, we thus jointly retrieve the obtained CBH from the 2B-CLDCLASS-LIDAR product, only considering cases where a surface observation was in the vicinity of the satellite track (inside a disc with a ~60 km radius around the surface observation, cf. section 2.3). For the samples fulfilling these conditions, we then compare how the different retrievals fare. In Figure 46, the joint histograms for the surface observations, the 2B-CLDCLASS-LIDAR retrieval and the method’s corresponding predictions are documented, representing a total of around 800 samples.

486 Investigating the joint histogram between the surface observations and the 2B-CLDCLASS-LIDAR retrievals (Fig. 64a) allows to identify shortcomings of the active satellite retrievals in particular close to the surface (Tanelli et al., 2008; Marchand et al., 2008). Indeed, the CBHs closer to the surface are not well captured by the 2B-CLDCLASS-LIDAR retrievals 2B-CLDCLASS-LIDAR retrievals closer to the surface are not well captured as partially expected, due to thick clouds attenuating the lidar signal, and due to ground clutter and lack of sensitivity to small droplets near cloud base for the radar signal. A similar explanation can eventually be articulated as a whole for the co-located retrievals, considering that the mean bias between the two retrievals is greater than + 600 m. Concurrently, it is fruitful to compare the 2B-CLDCLASS-LIDAR retrievals with the predictions from the developed method (Fig. 64b). As seen previously, ORABase the OR method struggles at higher CBHs, but agrees here reasonably well with the active satellite retrievals, especially for retrievals between 500 m and 1500 m.

495 Focusing on retrievals under 1.5 km, the prediction model achieves similar performance as presented in [Table 2](#) with a MAE of  
 496 488 m and a RMSE of 576 m, even though the subset here is much smaller.  
 497 Furthermore, we created a more extensive dataset using only 2B-CLDCLASS-LIDAR retrievals and the cloud scene predictions  
 498 with the aim of obtaining a more complete view of the relationship between these two retrievals. To this extent, we collated  
 499 around 160 000 samples of aligned cloud scene base height predictions and the 2B-CLDCLASS-LIDAR retrievals over the year  
 500 2016. For this dataset, the performance metrics exhibit similar values as on the previously presented subset, displaying even  
 501 lower values for the MAE and the absolute error standard deviation (around a 50 m decrease for both). Similarly to the previous  
 502 co-located subset, limiting the evaluation to lower cloud base retrievals yields performance metrics close to a 450 m MAE and a  
 503 270 m absolute error standard deviation, both of these being mainly impacted by agreeing retrievals in the 500 m to 1500 m  
 504 range.

**Joint histogram - Surface observations and model predictions**

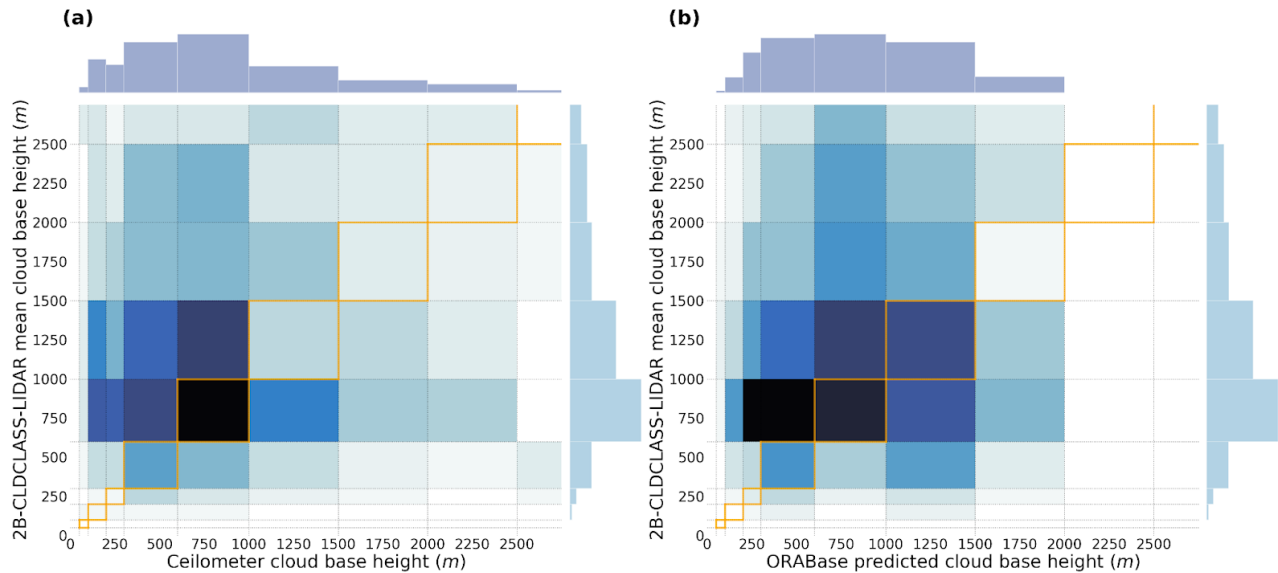


505  
 506  
 507 **Figure 35: Joint histogram over the test set of the surface observations and the predicted cloud scene base height from**  
 508 **ORABase with the ordinal regression all-threshold model. The 1:1 boxes are highlighted in orange in the figure.**

509 **4 Global distribution**

510  
 511 To further evaluate the method, we also apply the prediction model on global MODIS data for the whole year of 2016. The  
 512 sampling process yields approximately 700 000 CBH retrievals for the corresponding cloud properties tiles. ~~The final prediction~~  
 513 ~~model was beforehand re-trained on the whole co-located dataset including the test set of section 3.1.~~ We then spatially aggregate  
 514 the predictions to a regular grid of 5° and compute the annual mean per grid cell along the annual median absolute deviation  
 515 (MAD). ~~over the year and consider the spatial mean and median absolute deviation (MAD).~~ The MAD constitutes a useful metric  
 516 to quantify the variability while removing the effects of outliers. For more robust evaluation and statistics, only ocean grid cells  
 517 with more than 100 CBH retrievals over the year are displayed thus impacting mostly coastal and polar regions where filtering  
 518 for ocean-only scenes or the original amount of satellite retrievals leads to a higher rate of displaying removal. The spatial  
 519 distribution of the mean cloud base ([Fig. 75](#), top) is similar to the outlined global distributions from other studies using different  
 520 instruments and methods (Böhm et al., 2019; Lu et al., 2021; Mülmenstädt et al., 2018). ~~It is to be noted that~~ The illustrated  
 521 global quantities were established using MODIS overpasses which happen at a practically constant local time (13:30 h, early

522 afternoon for AQUA). The MAD pattern exhibits similar characteristics (Fig. 75, bottom), even though variability slightly  
 523 increases in the vicinity of land masses. These interpretations still remain valid when looking at relative deviations. Typical  
 524 features are lower cloud bases towards polar regions and the mid-latitudes, and higher ones in the tropical regions. One can  
 525 further observe regions like the pacific coast of South America or the Namibian coast which display lower cloud bases  
 526 concurrently with lower variability (also highlighted in Lu et al. (2021)). It is however impossible to follow up the study for  
 527 nighttime retrievals, as some MODIS cloud properties are not retrieved then.



528

529 **Figure 64: Joint histogram of (a) surface observations and 2B-CLDCLASS-LIDAR retrievals, and (b)**  
 530 **ORABaseML-model predictions and 2B-CLDCLASS-LIDAR retrievals, for the co-located cloud scenes during the year**  
 531 **2008. The 1:1 boxes are highlighted in the figure in orange.**

532

### 533 5 Conclusion

534

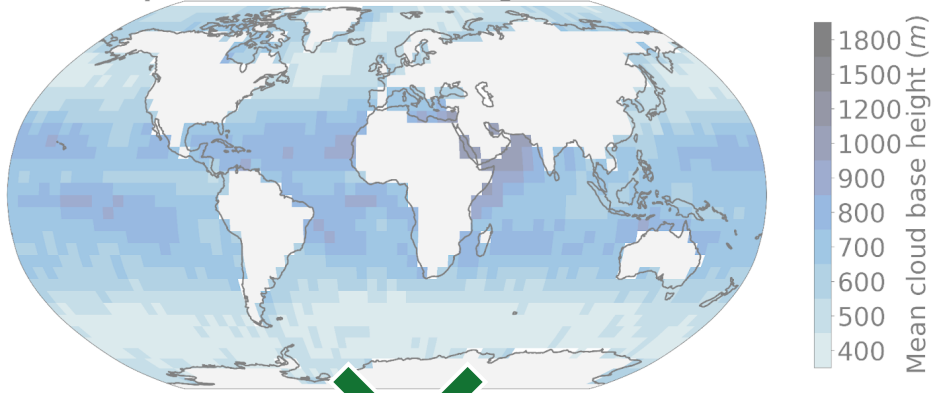
535 We have presented here a novel method named ORABase which retrieves the cloud scene base height over marine areas from  
 536 MODIS cloud properties, specifically CTH, COT and CWP. This method can produce robust CBH estimates for cloud scenes in  
 537 particular for lower cloud bases (MAE of 379 m and absolute error standard deviation of 328 m for up to 2 km cloud bases),  
 538 based on the assumption of a homogeneous cloud base across the considered cloud field. The statistical model was built on  
 539 surface observations of cloud bases with ceilometers (section 2.1), and then evaluated in comparison to other methods using  
 540 passive satellite instruments (section 3.1) and active satellite retrievals (section 3.2). Analysis of the yearly averaged CBH  
 541 (section 4) helped to further make sense of the predicted cloud bases and variability. The global dataset for the year 2016 is  
 542 available from Zenodo (Lenhardt et al., 2024).

543 Using the spatially-resolved information of cloud fields of CTH, COT and CWP through the described CNN-AE results in more  
 544 accurate CBH retrievals compared to the active retrievals of the 2B-CLDCLASS-LIDAR product, producing better performance  
 545 metrics compared to the other products and methods considered in this study. ~~with passive satellites allows to properly quantify~~  
 546 ~~lower cloud bases, more specifically avoiding the noisy retrievals of active satellites closer to the surface. A CNN proves to be~~  
 547 ~~valuable to leverage spatial information without making any assumption with respect to how the cloud quantities are related to~~  
 548 ~~the CBH.~~ The combination of a CNN based AE to reduce the dimensionality of the spatial patterns of cloud properties followed  
 549 by a simple OR model leads to a better CBH retrieval compared to previous presented methods. The OR modelisation helps  
 550 bridging the gap between regression and classification, facilitating the use of the binned cloud base observations provided by the  
 551 surface observation dataset. Overall, ~~ORABaseML-model~~ achieves low error in the retrievals, around 400 m, and  
 552 concurrently a narrow absolute error distribution, more precisely around 400 m absolute error standard deviation. Both of these  
 553 performance metrics are additionally reduced when focusing on cloud bases lower than 2 km. Application to data over land areas  
 554 has not been processed yet but would certainly require adding surface observations from land during the training process (e.g.  
 555 Böhm et al., 2019; Lu et al., 2021; Mülmenstädt et al., 2018). Application of the presented retrieval method to other instruments  
 556 could also be considered. Incorporating TERRA MODIS data would help constrain the annual mean estimates presented in  
 557 Figure 5 by partially removing the potential bias of the single daily overpass arising from using only AQUA data presented in  
 558 this study. The aspect enabling potential application of the retrieval method to different instruments outside of the two MODIS

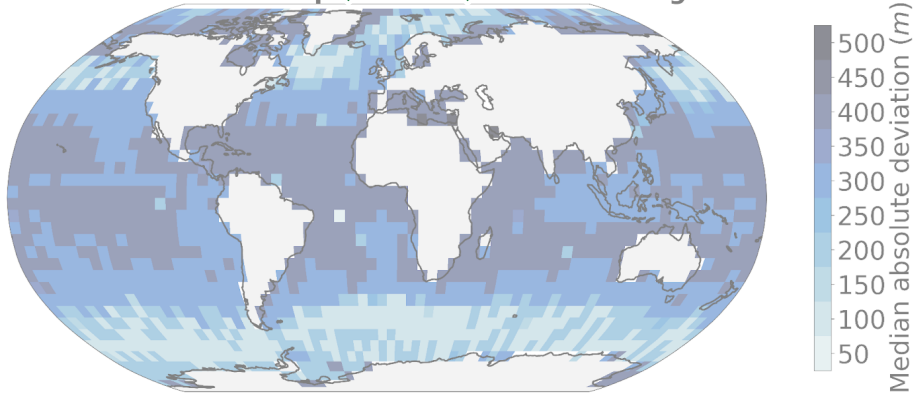


559 sensors would be the standardisation process for the input cloud properties before the use of the AE which is done based on  
560 means and standard deviations computed from AQUA-only granules. Carefully investigating the characteristics of the  
561 distribution of the cloud properties from another instrument to ensure proper scaling when using the trained AE would be then  
562 necessary. Further tests could be additionally done using coarser resolution for the input cloud properties.  
563 Furthermore, classical semi-supervised pipelines like the one presented here, characterised by a small labelled dataset and a vast  
564 unlabelled dataset, necessitate a kind of co-location or matching process which often proves to be cumbersome and generates  
565 only a limited amount of labels. However, future avenues of research could consider directly modelling unmatched datasets, as in  
566 e.g. Lun Chau et al. (2021) with multiresolution atmospheric data, by making use of other quantities present in the observations  
567 as mediating variables to model the link between observed and unobserved variables.  
568 In essence, the main benefit of producing better cloud base estimates is to gain accuracy in the overall retrieval of cloud  
569 geometry, impacting in particular radiation estimates (Kato et al., 2011) like the surface downwelling longwave radiation  
570 (Mülmenstädt et al., 2018). ~~ORABase~~ Our method can thus prove to be useful by helping to produce CBH with enhanced  
571 confidence at a global scale.  
572

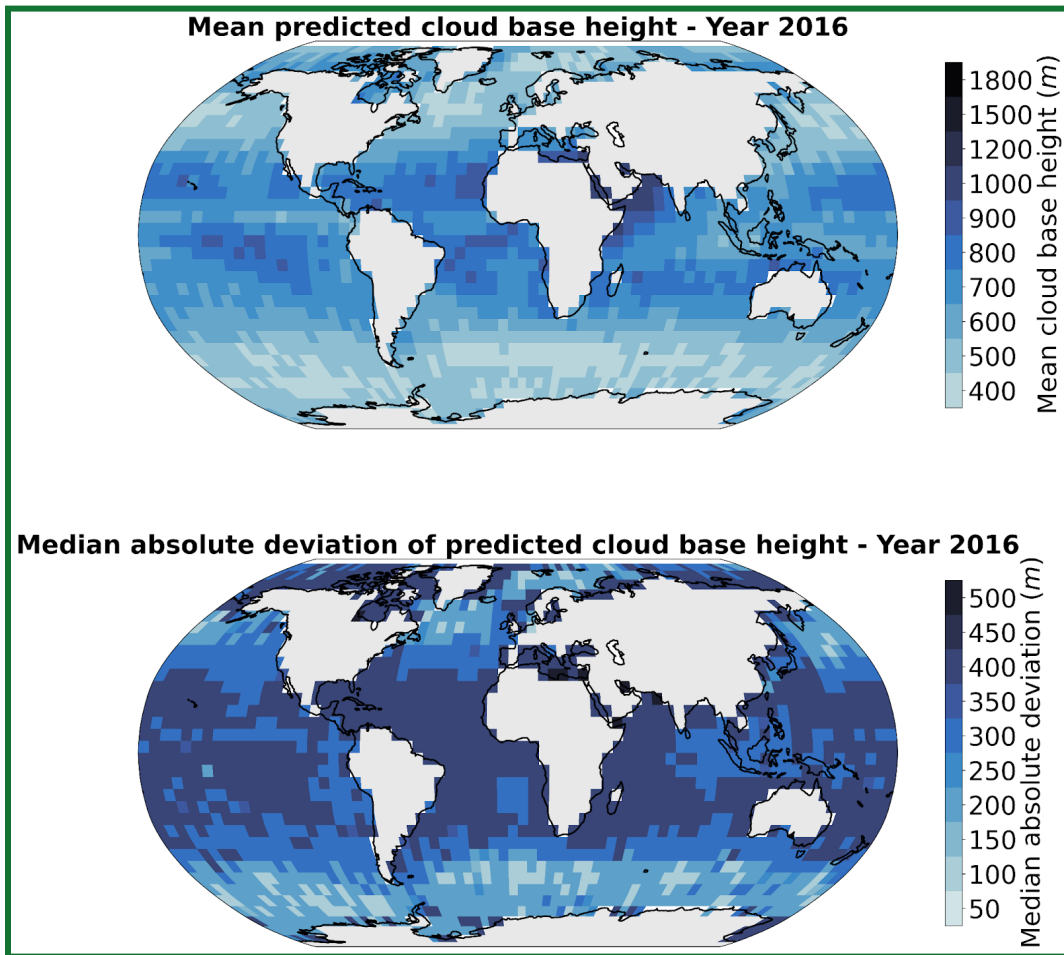
Mean predicted cloud base height - Year 2016



Median absolute deviation of predicted cloud base height - Year 2016



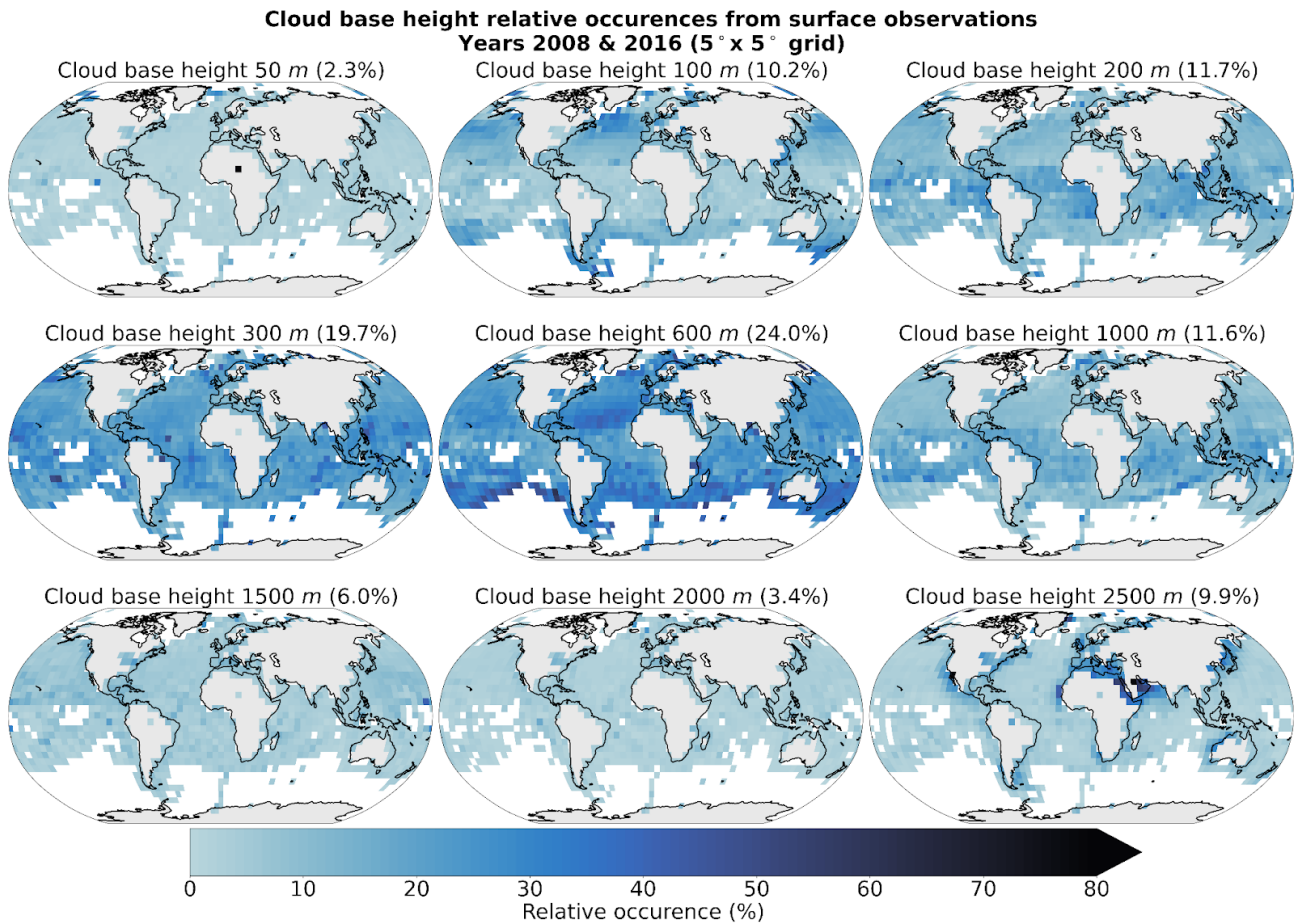
573



574

575 **Figure 75: Spatial distribution of (top) mean and (bottom) median absolute deviation of predicted cloud base height for**  
 576 **the MODIS data of the year 2016 aggregated on a 5 ° grid.**

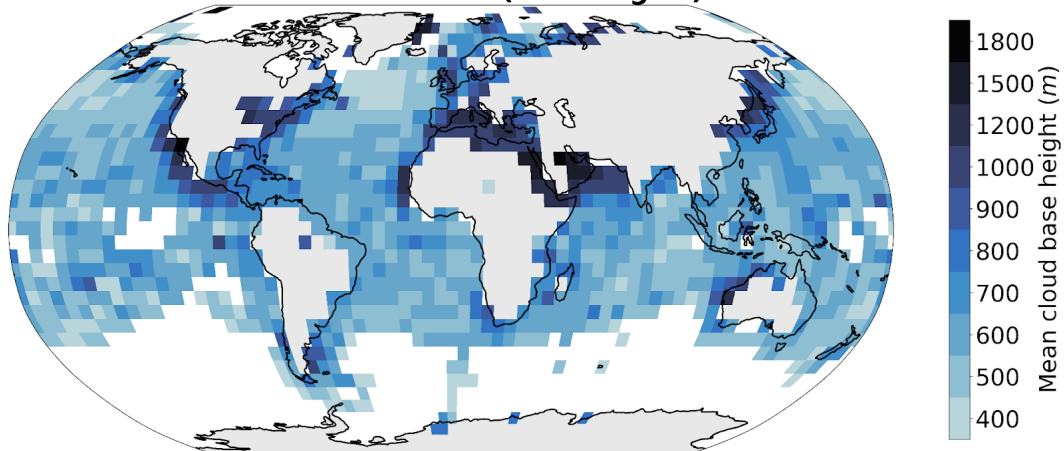
579 Appendix A: Cloud base height retrievals distribution



580

581 Figure A.1: Spatial distribution of cloud base height retrievals (Met Office, 2006) for the years 2008 and 2016 on a 5°  
582 grid. Overall percentage of each label in the total observations is indicated in brackets. Only grid cells with more than 10  
583 retrievals are displayed.

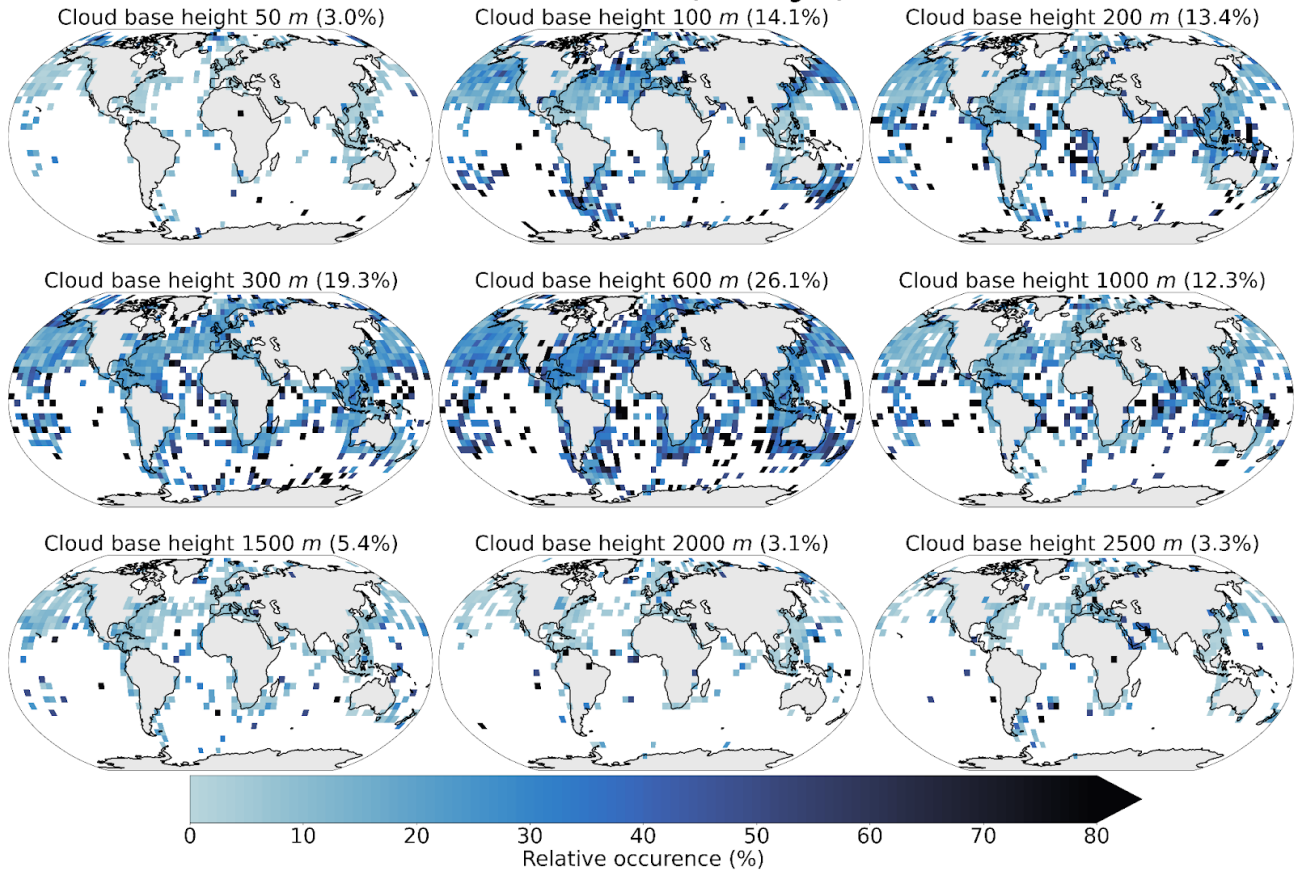
**Mean cloud base height from surface observations**  
**Years 2008 & 2016 (5° x 5° grid)**



584

585 Figure A.2: Mean cloud base height from retrievals (Met Office, 2006) for the years 2008 and 2016 on a 5° grid. Only  
586 grid cells with more than 50 retrievals are displayed.  
587

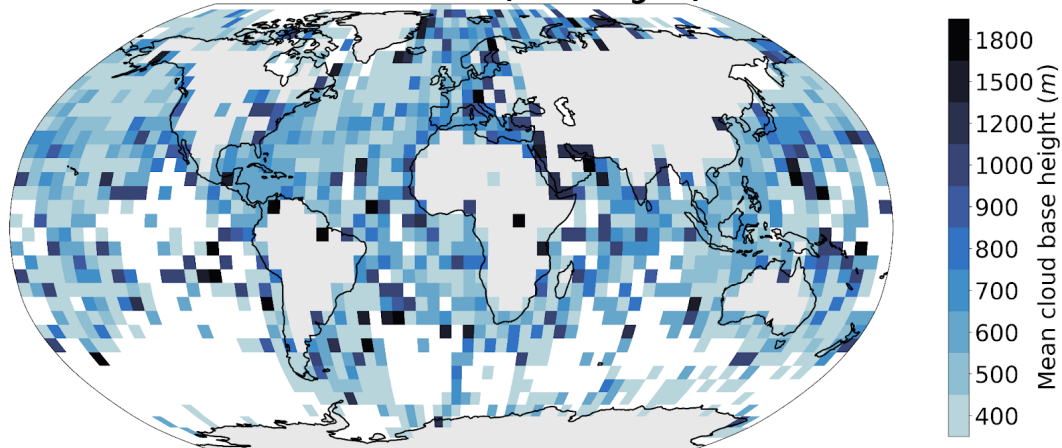
**Cloud base height relative occurrences for the co-located input dataset  
Years 2008 & 2016 (5° x 5° grid)**



588

589 **Figure A.3: Spatial distribution of the co-located cloud base height retrievals (Met Office, 2006) and the satellite cloud**  
 590 **properties used for training the prediction model for the years 2008 and 2016 on a 5° grid. Overall percentage of each**  
 591 **label in the total dataset is indicated in brackets.**  
 592

**Mean cloud base height for the co-located input dataset  
Years 2008 & 2016 (5° x 5° grid)**



593

594

595 **Figure A.4: Mean cloud base height from the co-located retrievals (Met Office, 2006) and the satellite cloud**  
 596 **properties used for training the prediction model for the years 2008 and 2016 on a 5° grid.**

## 597 Appendix B: Spatio-temporal correlation study

598

599 We create five different datasets to evaluate how the chosen AE architecture is capable of generalising to new data while trying  
600 to remove some possible autocorrelation biases which might inflate the performance scores. We also use this study to analyse  
601 how the AE model behaves when trained with our input data. We define two splits for space and time in order to build the  
602 training and testing datasets, namely the South-western (SW) quadrant and the period from March to October, respectively. The  
603 *granuleswath*s used to build the datasets span across the whole year of 2016. The *random* data split is the basis for the training of  
604 the model and consists of tiles sampled in the aforementioned quadrant and time period. These tiles are then split randomly  
605 between training, validation and testing datasets. This split represents the common way of splitting data when building a ML  
606 model. In contrast, we build 3 other datasets which vary through their respective spatial and time spans. The *spatial* split is built  
607 considering tiles spanning across a distinct time period, here between November and February, regardless of their spatial  
608 location. The *temporal* split is built considering tiles located anywhere but in the South-western quadrant regardless of the time  
609 at which the retrieval occurred. Finally the *spatio-temporal* split combines the previous two conditions in order to build a dataset  
610 in which the tiles come from an independent location and time as the ones used for training. Additionally, we create a global data  
611 split using data from a different year, here 2008, without any spatial restriction for the tiles. Furthermore, only a limited number  
612 of tiles was extracted from each *granuleswath*-file while only *granuleswath*s from non-consecutive days were used in order to  
613 limit possible correlation between the extracted scenes.

Data split	Time period	Spatial extent	<i>n</i>
Random	03-10.2016	SW quadrant	Train: 14 691 Validation: 4 198 Test: 2 099
Spatial	03-10.2016	Global except SW quadrant	107 736
Temporal	01-02 and 11-12.2016	SW quadrant	12 420
Spatio-temporal	01-02 and 11-12.2016	Global except SW quadrant	30 659
Global	12.2008	Global	7 111

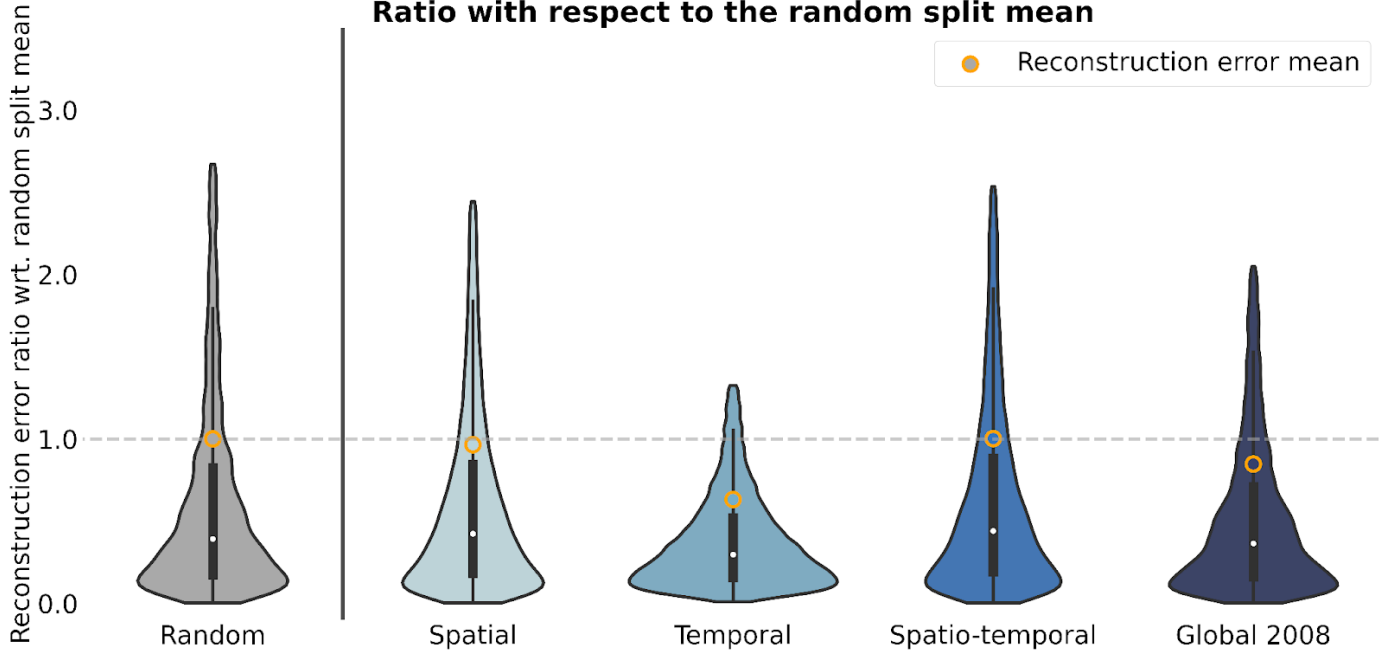
614 **Table B.1 : Name, time period, spatial extent and number of samples for each of the five described data splits.**

615

616 We then train an AE model using the training data from the first data split (*random*). Each test data split is then used to evaluate  
617 the trained model through the reconstruction errors divided by the reconstruction error mean of the *random* split (noted as  
618 reconstruction error ratio;  $\rightarrow$ (Fig. B.1)). Spatial distribution of the mean reconstruction errors is shown in [Figure B.2](#). We detail in  
619 [Table B.2](#) the average channel reconstruction error for each of the splits.

620 We first notice that the reconstruction power of the model is consistent regardless of the test split considered with mean  
621 reconstruction error ratios ranging from 0.63 to 1.0, dividing the split's reconstruction error by the random data split mean  
622 reconstruction error. Ratios around 1 or below indicate that the model's performance is not inflated when considering a random  
623 data split, highlighting that the model did not only learn from possible spatial and/or temporal correlations between samples  
624 present in the training set. The distribution of the error is also very similar throughout the test splits with most of the samples  
625 located below an error ratio of 0.5. However, one of the main aspects regarding the performance of the model across test splits is  
626 the presence of a heavy tail in the distribution showcasing that for some samples the reconstruction error can be greater than 3  
627 times the mean error. Looking at the spatial patterns of the reconstruction error, we note that overall the error comes from the  
628 COT and CWP predictions, the average reconstruction errors across test sets being 0.15, 0.32 and 0.25 for CTH, COT and CWP  
629 respectively ([Table B.2](#)). For the CTH, the error is concentrated in the zones with frequent convection around the equator and  
630 could be explained by local convection cells exhibiting a larger spread in CTH values. Another source of error could be that  
631 higher CTH values are also less represented in the training data. On the contrary, the error for COT and CWP is prevailing in  
632 high-latitude regions. Overall, the performance skill of the AE model seems to hold through the different test data splits. One  
633 could argue that the training dataset already retains enough variability in the data which could explain why the model still  
634 performs well regardless of the test set split. However, this consistent skill also shows that the performance reported in appendix  
635 C on the test set can be trusted to hold for other datasets and supports the data generation process to train the AE (cf. section 2.4).

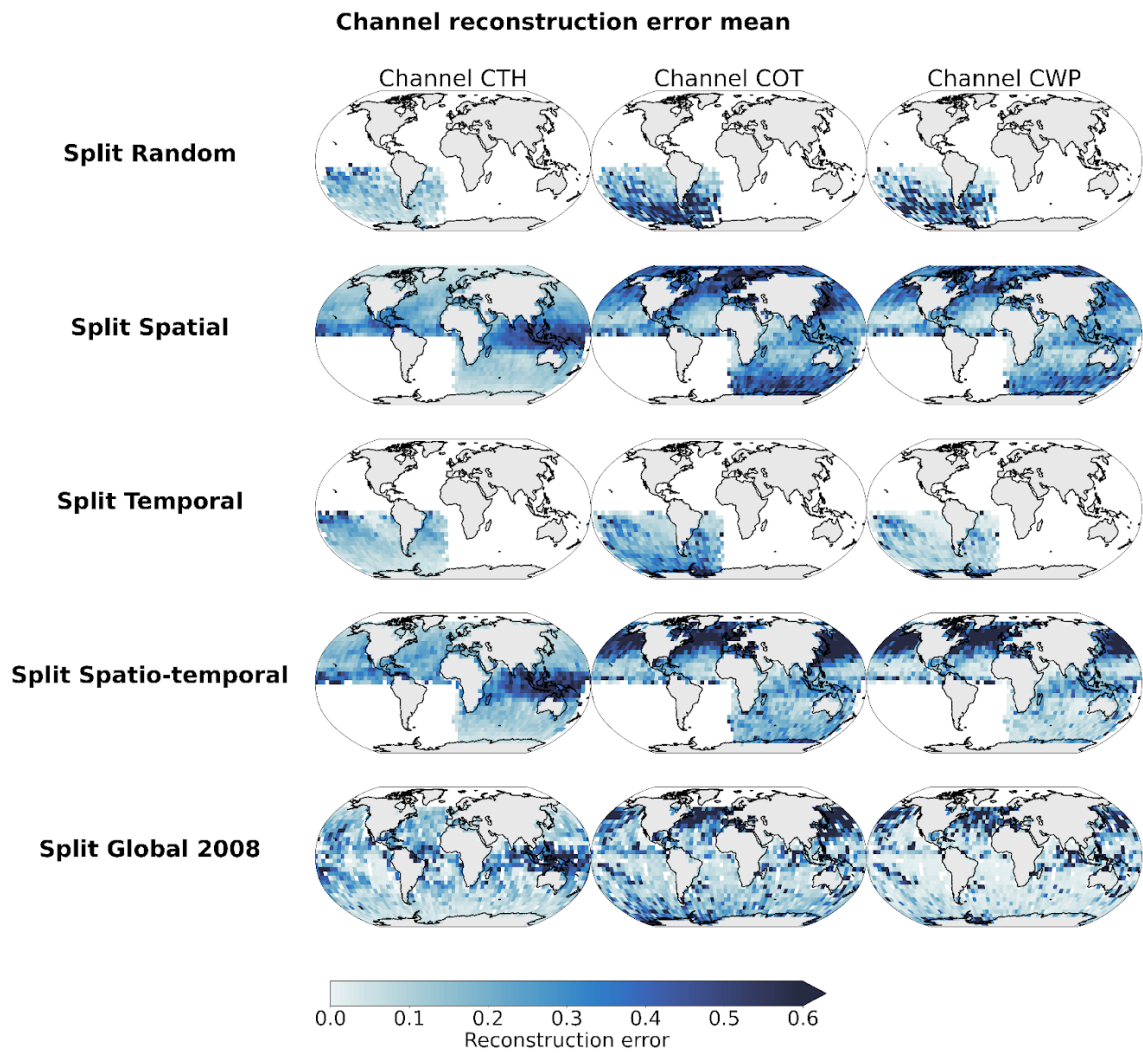
**Autoencoder reconstruction error distribution on different test sets  
Ratio with respect to the random split mean**



636  
637 **Figure B.1: Reconstruction error ratios of an AE on different test datasets. The quartiles are indicated with the barplot**  
638 **inside each violin plot while the mean is indicated with an orange circle. Extreme values were removed before plotting.**  
639 **Each sample's reconstruction error is divided by the mean reconstruction error of the random data split and defines the**  
640 **reconstruction error ratio presented here.**  
641

Data split	Channel			Average
	CTH	COT	CWP	
Random	0.117	0.369	0.333	0.273
Spatial	0.171	0.344	0.276	0.263
Temporal	0.114	0.253	0.150	0.172
Spatio-temporal	0.202	0.332	0.286	0.274
Global	0.154	0.318	0.221	0.231
Average	0.152	0.323	0.253	0.243

642 **Table B.2 : Average channel reconstruction relative error for each of the five described data splits.**  
643



644  
645

**Figure B.2: Distribution of mean channel reconstruction errors aggregated on a 5 ° grid.**



646 **Appendix C: Autoencoder architecture, training and performance**

647

648 The two components of the AE model, namely the encoder and the decoder, consist of five convolution blocks. Each block is  
 649 then made of three convolution operators followed by LeakyReLU activation functions (Maas et al., 2013). After the last  
 650 convolution of each block, batch normalisation is added to help convergence (Ioffe et al., 2015) followed by a maximum pooling  
 651 layer. We then add linear layers to enforce the desired dimension of the latent space. The decoder architecture follows the same  
 652 principles with transposed convolution layers (Zeiler et al., 2010) replacing the pooling layers of the encoder. This is summarised  
 653 in [Table C.1](#). Details about the training of the AE are included in [Table C.2](#) and the loss history during training is shown in  
 654 [Figure C.1](#).

Layer	Hyperparameters	Output shape
<b>Input</b>		(None, 3, 128, 128)
<b>Encoder</b>		
Conv2d	(kernel = 3, stride = 2)	(None, 3, 64, 64)
ConvBlock x 5	Conv2d (kernel = 3, stride = 1) LeakyReLU Conv2d (kernel = 3, stride = 1) LeakyReLU Conv2d (kernel = 3, stride = 1) BatchNorm2d LeakyReLU MaxPool2d (kernel = 2, stride = 2)	(None, 256, 2, 2)
Flatten + Linear		(None, 256)
<b>Decoder</b>		
Linear + Unflatten		(None, 256, 2, 2)
ConvTranspose2d	(kernel = 2, stride = 2)	(None, 256, 4, 4)
ConvTransposeBlock x 5	Conv2d (kernel = 3, stride = 1) LeakyReLU Conv2d (kernel = 3, stride = 1) LeakyReLU Conv2d (kernel = 3, stride = 1) BatchNorm2d LeakyReLU ConvTranspose2d (kernel = 2, stride = 2)	(None, 3, 128, 128)

655

**Table C.1 : Autoencoder model specifications.**

656

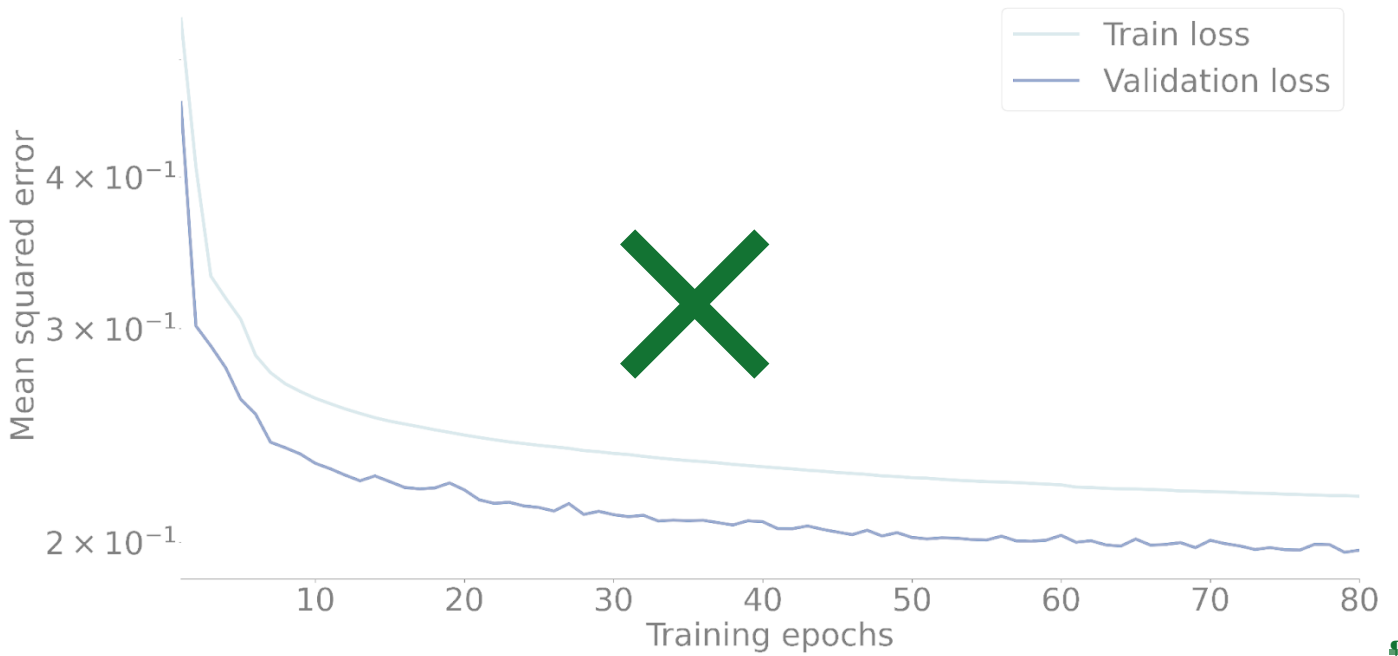
Hyperparameter	Value
Batch size	64
Epochs	80
Optimizer	Stochastic Gradient Descent (SGD), momentum = 0.9, learning rate = 0.0001
Metric	MSE
Early stopping	patience = 20

657

Table C.2 : Autoencoder model training specifications.

658

### Autoencoder train/validation loss



659

660

Figure C.1 : Training and validation losses during model optimization.

## 661 Appendix D: Ordinal regression

662

663 We define our labels  $y$  which can take values in  $K = 9$  classes from  $\{50 \text{ m}, 100 \text{ m}, \dots, 2500 \text{ m}\}$ . We introduce  $K - 1$   
664 thresholds  $\alpha_y$  to define the separation of our  $K$  classes which actually correspond here to the classes too. For each labelled  
665 sample  $(s, y)$  the output of our model is  $z = z(s)$ . The correct interval for this ~~this~~ sample is then  $(\alpha_{y-1}, \alpha_y)$   ~~$(\alpha_{y-1}, \alpha_y)$~~ .

666 During the fitting process, the goal is to find the set of parameters of our model  $z$  and the corresponding thresholds  $\alpha$  which  
667 minimises a certain cost function. We consider a generic nonnegative penalisation function  $f(\cdot)$  (eg. hinge loss, squared error  
668 loss, Huber loss). There are then different ways to represent threshold violations and thus to penalise the predictor. While  
669 immediate-threshold setup only considers the thresholds of the correct interval, all-threshold setup takes into account all the  
670 threshold violations. In the case of an immediate-threshold setup the loss function would look like:

$$671 \quad \mathcal{L}(z, y) = f(z - \alpha_{y-1}) + f(\alpha_y - z); \quad (\text{D.1})$$

672 Here we can see that the loss is not aware of how many thresholds are actually violated. In the case of an all-threshold setup the  
673 loss function is a sum of violations across all thresholds:

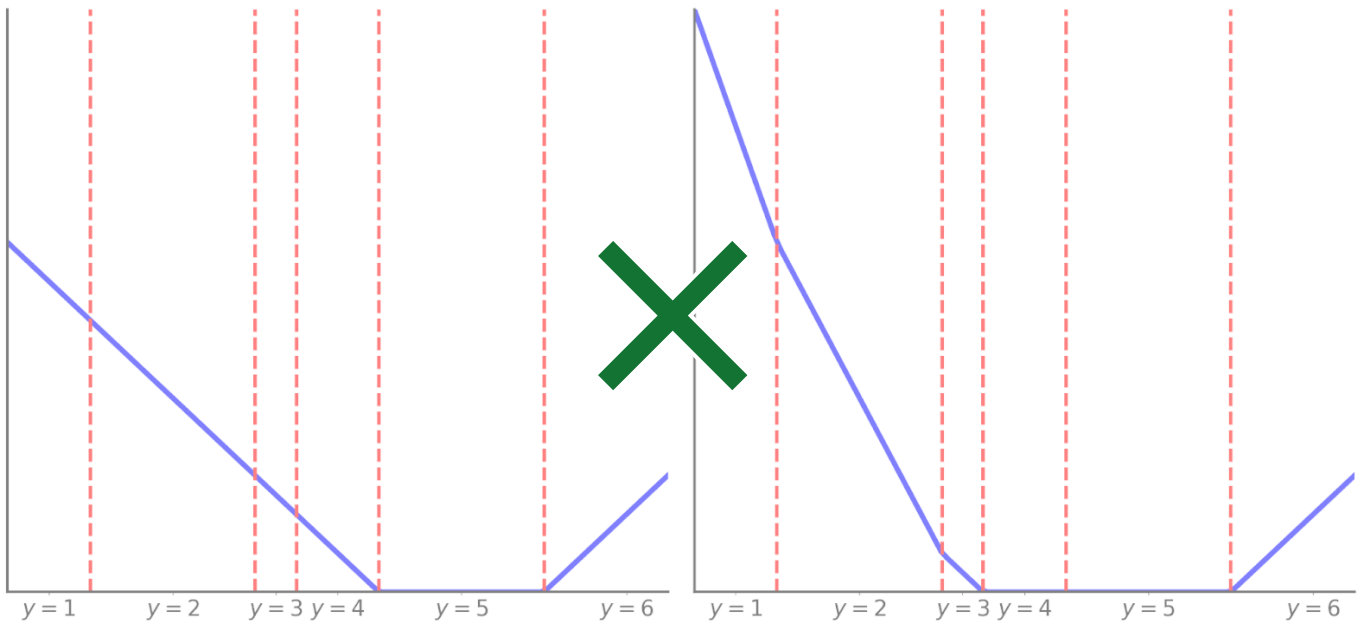
$$674 \quad \mathcal{L}(z, y) = \sum_{i=1}^{K-1} f(t(i, y)(\alpha_{iy} - z)) \quad (\text{D.2});$$

675 where  $t(i, y) = -1$  if  $i < y$  or  $+1$  if  $i \geq y$ . Thus predictions are encouraged to violate the least amount of thresholds.

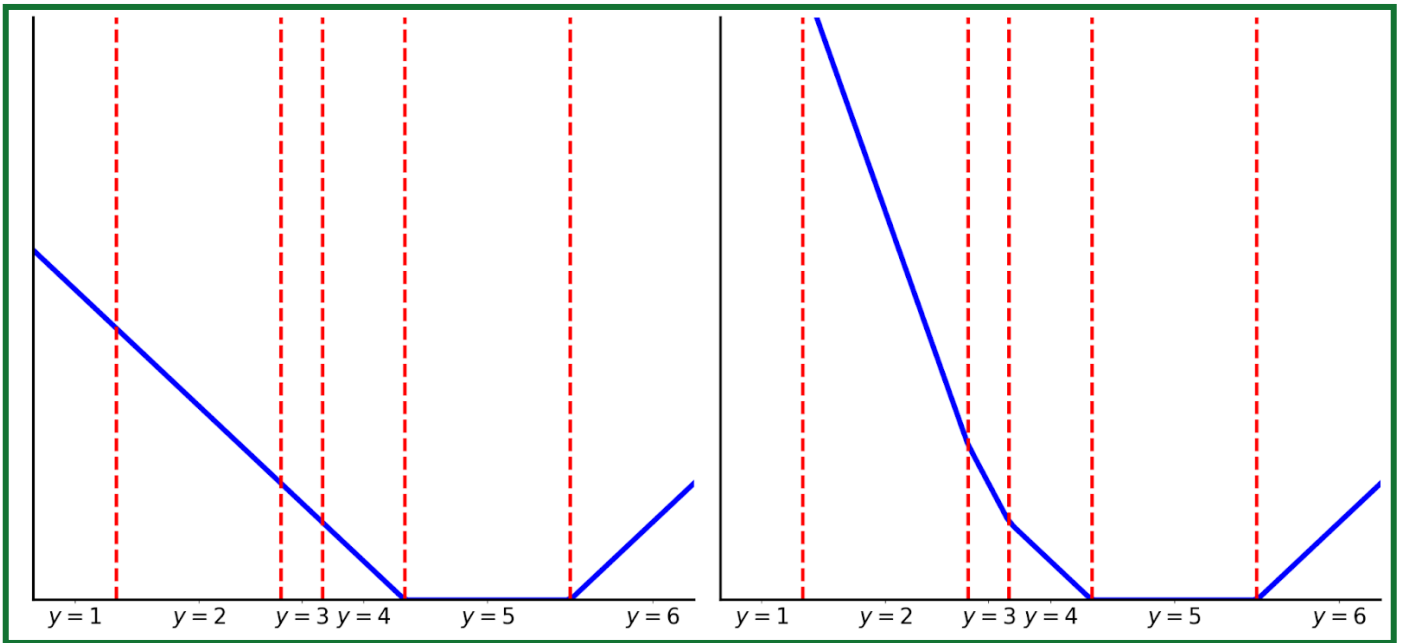
676 We give in [Figure D.1](#) an example of what the loss function would look like in the case of  $K = 6$  labels and using a hinge  
677 penalisation.

678

679



680



681 **Figure D.1: Threshold-based setups loss function representation for a hinge penalisation,  $K=6$  labels and target label  $y=5$ .**  
682 **(left) Immediate-threshold and (right) All-threshold setup loss function. (figure adapted from Rennie et al. (2005))**

683 **Appendix E: Cloud base height retrieval method assuming adiabatic cloud**

684

685 Algorithm adapted from Goren et al. (2018). We use the retrieved CTH, CTT, CTP and CWP from MODIS MYD06 (Platnick et  
686 al., 2017).

687

---

**Algorithm:** Cloud base height retrieval

---

**Data:** CTH, CTT, CTP, LWP, look-up tables

**Result:** CBH

**if** CTT < 263.13 **then**

**return** NaN

T  $\leftarrow$  CTT - 273.13

LWP obs  $\leftarrow$  LWP

LWP adi  $\leftarrow$  0.

$\delta z \leftarrow$  0.

Set corresponding cloud top indexes for temperature  $T_{ind}$  and pressure  $p_{ind}$  look-up tables.

Read-in the water mixing ratio  $w$  at the corresponding indexes.

**if**  $w$  out of look-up table **then**

**return** NaN

**while** LWP adi < LWP obs **then**

$\rho_{tmp} \leftarrow$  density look-up table with  $T_{ind}$  and  $p_{ind}$

$\delta_{tmp} \leftarrow$  layer depth look-up table with  $T_{ind}$  and  $p_{ind}$

$\delta z \leftarrow \delta z + \delta_{tmp}$

$w_{tmp} \leftarrow$  mixing ratio look-up table with  $T_{ind}$  and  $p_{ind}$

    LWP adi  $\leftarrow$  LWP adi +  $(w_{tmp} - w) \times \delta z_{tmp} \times \rho_{tmp}$

    Adjust temperature T given the saturated lapse rate using look-up table with  $T_{ind}$  and  $p_{ind}$

    Update indexes  $T_{ind}$  and  $p_{ind}$

**return** CTH -  $\delta z$

---

688

689 **Table E.1: Pseudo code for cloud base height retrieval algorithm assuming adiabatic cloud, adapted from Goren et al.**  
690 **(2018).**

## 691 Code availability

692  
693 The code used for the method and producing the plots is available on Zenodo (Lenhardt et al., 2024).

## 694 Data availability

695  
696 The global dataset of the cloud base height predictions for the year 2016 is available on Zenodo (Lenhardt et al., 2024). The  
697 dataset is available as a csv file with corresponding coordinates, MODIS ~~granules~~ ~~swath file~~, time of retrieval and predicted cloud  
698 base height or in a netCDF file as daily aggregates on a regular grid with a resolution of 1° or 5°. The meteorological  
699 observations from the UK MetOffice (Met Office, 2006) are available through the CEDA archive at  
700 <https://catalogue.ceda.ac.uk/uuid/77910bcec71c820d4c92f40d3ed3f249>. The files from the CUMULO dataset (Zantedeschi et  
701 al., 2019) are available at <https://www.dropbox.com/sh/i3s9q2v2jyyk2it/AACxXnXfMF5wuIqLXqH4NJOra?dl=0>.

## 702 Author contribution

703  
704 JL, JQ and DS designed the study. JL wrote the code. JL conducted the analysis and JL, JQ, DS interpreted the results. JL  
705 prepared the manuscript, JQ and DS reviewed the manuscript and provided comments.

## 706 Competing interests

707  
708 The authors declare that they have no conflict of interest.

## 709 Acknowledgements

710  
711 This work was supported by the European Union's Horizon 2020 research and innovation programme under Marie  
712 Skłodowska-Curie grant agreement No. 860100 (iMIRACLI). We thank the Leipzig University Scientific Computing cluster for  
713 computing and data hosting. We further thank Tom Goren for providing access to code snippets from Goren et al. (2018) and  
714 thank Olivia Linke for helping review the manuscript. We acknowledge the contributors of the CUMULO dataset (Zantedeschi et  
715 al., 2019) for providing access to the data files hosted at  
716 <https://www.dropbox.com/sh/i3s9q2v2jyyk2it/AACxXnXfMF5wuIqLXqH4NJOra?dl=0>. Additionally, we acknowledge the  
717 MODIS L2 Cloud product data set from the Level-1 and Atmosphere Archive and Distribution System (LAADS) Distributed  
718 Active Archive Center (DAAC), located in the Goddard Space Flight Center in Greenbelt, Maryland  
719 ([https://ladsweb.modaps.eosdis.nasa.gov/archive/allData/61/MYD06\\_L2/](https://ladsweb.modaps.eosdis.nasa.gov/archive/allData/61/MYD06_L2/)). *We would like to thank two anonymous reviewers for*  
720 *their constructive and detailed comments.*

## 721 References

722

723 Ackerman, S. A., and Frey, R.: MODIS Atmosphere L2 Cloud Mask Product (35\_L2), NASA MODIS Adaptive Processing  
724 System, Goddard Space Flight Center, [http://doi.org/10.5067/MODIS/MOD35\\_L2.061](http://doi.org/10.5067/MODIS/MOD35_L2.061),  
725 [http://doi.org/10.5067/MODIS/MYD35\\_L2.061](http://doi.org/10.5067/MODIS/MYD35_L2.061), 2017.

726

727 Baccianella, S., Esuli, A. and Sebastiani, F.: Evaluation Measures for Ordinal Regression, Ninth International Conference on  
728 Intelligent Systems Design and Applications, Pisa, Italy, 283-287, <https://doi.org/10.1109/ISDA.2009.230>, 2009.

729

730 Baldi, P.: Autoencoders, Unsupervised Learning, and Deep Architectures, in: Proceedings of the International Conference on  
731 Machine Learning (ICML), Workshop on Unsupervised and Transfer Learning, Proceedings of Machine Learning Research,  
732 Volume 27, 37-49, <https://proceedings.mlr.press/v27/baldi12a.html>, 2012.

733

734 Baum, B.A., Menzel, W. P., Frey, R. A., Tobin, D. C., Holz, R. E., Ackerman, S. A., Heidinger, A. K., and Yang, P.: MODIS  
735 Cloud-Top Property Refinements for Collection 6, *Journal of Applied Meteorology and Climatology*, 51, 6, 1145-1163,  
736 <https://doi.org/10.1175/JAMC-D-11-0203.1>, 2012.

737

738 Böhm, C., Sourdeval, O., Mülmenstädt, J., Quaas, J., and Crewell, S.: Cloud base height retrieval from multi-angle satellite data,  
739 *Atmos. Meas. Tech.*, 12, 1841-1860, <https://doi.org/10.5194/amt-12-1841-2019>, 2019.

740

741 Boucher, O., Randall, D., Artaxo, P., Bretherton, C., Feingold, G., Forster, P., Kerminen, V.-M., Kondo, Y., Liao, H., Lohmann,  
742 U., Rasch, P., Satheesh, S. K., Sherwood, S., Stevens, B. and Zhang, X. Y.: Clouds and aerosols, *Climate Change 2013: The*  
743 *Physical Science Basis. Contribution of Working Group I to the Fifth Assessment Report of the Intergovernmental Panel on*  
744 *Climate Change*, 571-657, <https://doi.org/10.1017/CBO9781107415324.016>, 2013.

745

746 Cardoso, J. S. and Sousa, R.: Measuring the performance of ordinal classification, *International Journal of Pattern Recognition*  
747 *and Artificial Intelligence*, Volume 25, 8, 1173-1195, <https://doi.org/10.1142/S0218001411009093>, 2011.

748

749 Forster, P., T. Storelvmo, K. Armour, W. Collins, J.-L. Dufresne, D. Frame, D.J. Lunt, T. Mauritsen, M.D. Palmer, M. Watanabe,  
750 M. Wild, and H. Zhang: The Earth's Energy Budget, Climate Feedbacks, and Climate Sensitivity, in *Climate Change 2021: The*  
751 *Physical Science Basis. Contribution of Working Group I to the Sixth Assessment Report of the Intergovernmental Panel on*  
752 *Climate Change [Masson-Delmotte, V., P. Zhai, A. Pirani, S.L. Connors, C. Péan, S. Berger, N. Caud, Y. Chen, L. Goldfarb, M.I.*  
753 *Gomis, M. Huang, K. Leitzell, E. Lonnoy, J.B.R. Matthews, T.K. Maycock, T. Waterfield, O. Yelekçi, R. Yu, and B. Zhou (eds.)].*  
754 *Cambridge University Press, Cambridge, United Kingdom and New York, NY, USA*, pp. 923–1054,  
755 <http://doi.org/10.1017/9781009157896.009>, 2021.

756

757 Goldberg, M. D., Kilcoyne, H., Cikanek, H., and Mehta, A.: Joint Polar Satellite System: The United States next generation  
758 civilian polar-orbiting environmental satellite system, *J. Geophys. Res. Atmos.*, 118, 13,463–13,475,  
759 <https://doi.org/10.1002/2013JD020389>, 2013.

760

761 Goren, T., Rosenfeld, D., Sourdeval, O., and Quaas, J.: Satellite Observations of Precipitating Marine Stratocumulus Show  
762 Greater Cloud Fraction for Decoupled Clouds in Comparison to Coupled Clouds, *Geophys. Res. Lett.*, 45, 5126–5134,  
763 <https://doi.org/10.1029/2018GL078122>, 2018.

764

765 Grosvenor, D. P., Sourdeval, O., Zuidema, P., Ackerman, A., Alexandrov, M. D., Bennartz, R., Boers, R., Cairns, B., Chiu, J. C.,  
766 Christensen, M., Deneke, H., Diamond, M., Feingold, G., Fridlind, A., Hünerbein, A., Knist, C., Kollias, P., Marshak, A.,  
767 McCoy, D., Merk, D., Painemal, D., Rausch, J., Rosenfeld, D., Russchenberg, H., Seifert, P., Sinclair, K., Stier, P., van  
768 Diedenhoven, B., Wendisch, M., Werner, F., Wood, R., Zhang, Z. and Quaas, J.: Remote sensing of droplet number concentration  
769 in warm clouds: A review of the current state of knowledge and perspectives, *Reviews of Geophysics*, 56, 409–453,  
770 <https://doi.org/10.1029/2017RG00059>, 2018.

771

772 Gutiérrez, P. A., Pérez-Ortiz, M., Sánchez-Monedero, J., Fernández-Navarro, F. and Hervás-Martínez, C.: Ordinal Regression  
773 Methods: Survey and Experimental Study, *IEEE Transactions on Knowledge and Data Engineering*, 28, 1, 127-146,  
774 <https://doi.org/10.1109/TKDE.2015.2457911>, 2016.  
775

776 Hinton, G.E., and Salakhutdinov, R.R.: Reducing the dimensionality of data with neural networks, *Science*, 313, 5786, 504-507,  
777 <https://doi.org/10.1126/science.1127647>, 2006.  
778

779 Hunt, W. H., Winker, D. M., Vaughan, M. A., Powell, K. A., Lucker, P. L., and Weimer, C.: CALIPSO Lidar Description and  
780 Performance Assessment. *J. Atmos. Oceanic Technol.*, 26, 1214–1228, <https://doi.org/10.1175/2009JTECHA1223.1>, 2009.  
781

782 Ioffe, S., and Szegedy, C.: Batch Normalization: Accelerating Deep Network Training by Reducing Internal Covariate Shift, in:  
783 *Proceedings of the 32nd International Conference on Machine Learning (ICML)*, *Proceedings of Machine Learning Research*,  
784 Volume 37, 448-456, <http://proceedings.mlr.press/v37/ioffe15.html>, 2015.  
785

786 Kato, S., Rose, F. G., Sun-Mack, S., Miller, W. F., Chen, Y., Rutan, D. A., Stephens, G. L., Loeb, N. G., Minnis, P., Wielicki, B.  
787 A., Winker, D. M., Charlock, T. P., Stackhouse, P. W. J., Xu, K.-M., and Collins, W. D.: Improvements of top-of-atmosphere and  
788 surface irradiance computations with CALIPSO-, CloudSat-, and MODIS-derived cloud and aerosol properties, *J. Geophys.*  
789 *Res.-Atmos.*, 116, D19209, <https://doi.org/10.1029/2011JD016050>, 2011.  
790

791 Kattenborn, T., Schiefer, F., Frey, J., Feilhauer, H., Mahecha, M. D., and Dormann, C. F.: Spatially autocorrelated training and  
792 validation samples inflate performance assessment of convolutional neural networks, *ISPRS Open Journal of Photogrammetry*  
793 *and Remote Sensing*, 5, 2667-3932, <https://doi.org/10.1016/j.ophoto.2022.100018>, 2022.  
794

795 Kramer, M.A.: Nonlinear principal component analysis using autoassociative neural networks, *AIChe J.*, Volume 37, 233-243,  
796 <https://doi.org/10.1002/aic.690370209>, 1991.  
797

798 Krizhevsky, A., Sutskever, I., and Hinton, G.: ImageNet Classification with Deep Convolutional Neural Networks, in:  
799 *Proceedings of Advances in Neural Information Processing Systems 25*, Annual Conference on Neural Information Processing  
800 Systems (NeurIPS), 1097-1105,  
801 [https://proceedings.neurips.cc/paper\\_files/paper/2012/file/c399862d3b9d6b76c8436e924a68c45b-Paper.pdf](https://proceedings.neurips.cc/paper_files/paper/2012/file/c399862d3b9d6b76c8436e924a68c45b-Paper.pdf), 2012.  
802

803 Lázaro, M, and Figueiras-Vidal, A. R.: Neural network for ordinal classification of imbalanced data by minimizing a Bayesian  
804 cost, *Pattern Recognition*, Volume 137, <https://doi.org/10.1016/j.patcog.2023.109303>, 2023.  
805

806 LeCun, Y., Jackel, L. D., Boser, B., Denker, J. S., Graf, H. P., Guyon, I., Henderson, D., Howard, R. E., and Hubbard, W.:  
807 Handwritten digit recognition: Applications of neural network chips and automatic learning, *IEEE Communications Magazine*,  
808 Volume 27, Issue 11, 41-46, <https://doi.org/10.1109/35.41400>, 1989.  
809

810 LeCun, Y., and Bengio, Y.: Convolutional networks for images, speech, and time series, *The handbook of brain theory and neural*  
811 *networks*, 3361, 10, 1995.  
812

813 LeCun, Y., Kavukcuoglu, K., and Farabet, C.: Convolutional networks and applications in vision, in: *Proceedings of 2010 IEEE*  
814 *International Symposium on Circuits and Systems*, 253-256, <https://doi.org/10.1109/ISCAS.2010.5537907>, 2010.  
815

816 Lenhardt, J., Quaas, J., and Sejdinovic, D.: Code and data for: Marine cloud base height retrieval from MODIS cloud properties  
817 using machine learning, *Zenodo*, <https://doi.org/10.5281/zenodo.10517687>, 2024.  
818

819 Lu, X., Mao, F., Rosenfeld, D., Zhu, Y., Pan, Z., and Gong, W.: Satellite retrieval of cloud base height and geometric thickness of  
820 low-level cloud based on CALIPSO, *Atmos. Chem. Phys.*, Volume 21, Issue 15, 11979-12003,  
821 <https://doi.org/10.5194/acp-21-11979-2021>, 2021.  
822



823 Lun Chau, S., Bouabid, S., and Sejdinovic, D.: Deconditional Downscaling with Gaussian Processes, in: Proceedings of  
824 Advances in Neural Information Processing Systems 34, Annual Conference on Neural Information Processing Systems  
825 (NeurIPS), <https://doi.org/10.48550/arXiv.2105.12909>, 2021.  
826

827 Maas, A. L., Hannun, A. Y. and Ng, A. Y.: Rectifier Nonlinearities Improve Neural Network Acoustic Models, in: Proceedings of  
828 the 30th International Conference on Machine Learning (ICML), Atlanta, Georgia, USA, Journal of Machine Learning Research  
829 (JMLR), Volume 28, 3, 2013.  
830

831 Marchand, R., Mace, G. G., Ackerman, T., and Stephens, G.: Hydrometeor detection using Cloudsat – An earth-orbiting 94-GHz  
832 cloud radar, *J. Atmos. Ocean. Technol.*, Volume 25, 519–533, <https://doi.org/10.1175/2007JTECHA1006.1>, 2008.  
833

834 Met Office: MIDAS: Global Marine Meteorological Observations Data, NCAS British Atmospheric Data Centre,  
835 <https://catalogue.ceda.ac.uk/uuid/77910bcec71c820d4c92f40d3ed3f249>, 2006.  
836

837 Mülmenstädt, J., Sourdeval, O., Henderson, D. S., L'Ecuyer, T. S., Unglaub, C., Jungandreas, L., Böhm, C., Russell, L. M., and  
838 Quaas, J.: Using CALIOP to estimate cloud-field base height and its uncertainty: the Cloud Base Altitude Spatial Extrapolator  
839 (CBASE) algorithm and dataset, *Earth System Science Data*, Volume 10, Issue 4, 2279–2293,  
840 <https://doi.org/10.5194/essd-10-2279-2018>, 2018.  
841

842 Nair, V., and Hinton, G. E.: Rectified linear units improve restricted boltzmann machines, in: Proceedings of the 27th  
843 International Conference on International Conference on Machine Learning (ICML'10), Haifa, Israel, 2010, 807–814,  
844 <https://www.cs.toronto.edu/%7Efritz/absps/reluICML.pdf>, 2010.  
845

846 Niu, Z., Zhou, M., Wang, L., Gao, X., and Hua, G.: Ordinal Regression with Multiple Output CNN for Age Estimation, IEEE  
847 Conference on Computer Vision and Pattern Recognition (CVPR), 4920–4928, <https://doi.org/10.1109/CVPR.2016.532>, 2016.  
848

849 Noh, Y., Forsythe, J. M., Miller, S. D., Seaman, C. J., Li, Y., Heidinger, A. K., Lindsey, D. T., Rogers, M. A., and Partain, P. T.:  
850 Cloud-Base Height Estimation from VIIRS. Part II: A Statistical Algorithm Based on A-Train Satellite Data, *Journal of*  
851 *Atmospheric and Oceanic Technology*, Volume 34, Issue 3, 585–598, <https://doi.org/10.1175/JTECH-D-16-0110.1>, 2017.  
852

853 Paszke, A., Gross, S., Massa, F., Lerer, A., Bradbury, J., Chanan, G., Killeen, T., Lin, Z., Gimelshein, N., Antiga, L., Desmaison,  
854 A., Kopf, A., Yang, E., DeVito, Z., Raison, M., Tejani, A., Chilamkurthy, S., Steiner, B., Fang, L., Bai, J. and Chintala, S.:  
855 PyTorch: An Imperative Style, High-Performance Deep Learning Library, in *Advances in Neural Information Processing*  
856 *Systems* 32 (NeurIPS), 8024–8035,  
857 <http://papers.neurips.cc/paper/9015-pytorch-an-imperative-style-high-performance-deep-learning-library.pdf>, 2019.  
858

859 Pedregosa, F.: Feature extraction and supervised learning on fMRI: from practice to theory, Université Pierre et Marie Curie,  
860 Paris VI, <https://theses.hal.science/tel-01100921>, 2015.  
861

862 Pedregosa, F., Bach, F., and Gramfort, A.: On the Consistency of Ordinal Regression Methods, *Journal of Machine Learning*  
863 *Research (JMLR)*, Volume 18, 55, 1–35, <http://jmlr.org/papers/v18/15-495.html>, 2017.  
864

865 Platnick, S., Ackerman, S. A., King, M. D., Meyer, K., Menzel, W. P., Holz, R. E., Baum, B. A., and Yang, P.: MODIS  
866 atmosphere L2 cloud product (06\_L2), NASA MODIS Adaptive Processing System, Goddard Space Flight Center,  
867 [http://doi.org/10.5067/MODIS/MYD06\\_L2.061](http://doi.org/10.5067/MODIS/MYD06_L2.061), 2017.  
868

869 Platnick, S., King, M.D., Ackerman, S.A., Menzel, W.P., Baum, B.A., Riedi, J.C., and Frey, R.A.: The MODIS cloud products:  
870 algorithms and examples from Terra, in: *IEEE Transactions on Geoscience and Remote Sensing*, Volume 41, Number 2, 459–473,  
871 <http://doi.org/10.1109/TGRS.2002.808301>, 2003.  
872

873 Pu, Y., Gan, Z., Henaio, R., Yuan, X., Li, C., Stevens, A., and Carin, L.: Variational Autoencoder for Deep Learning of Images,  
874 Labels and Captions, in: Proceedings of Advances in Neural Information Processing Systems 29, Annual Conference on Neural  
875 Information Processing Systems (NeurIPS), 2352-2360, <https://doi.org/10.48550/arXiv.1609.08976>, 2016.  
876

877 Reichstein, M., Camps-Valls, G., Stevens, B., Jung, M., Denzler, J., Carvalhais, N., and Prabhat: Deep learning and process  
878 understanding for data-driven Earth system science, *Nature*, 566, 195-204, <https://doi.org/10.1038/s41586-019-0912-1>, 2019.  
879

880 Rennie, J.D., and Srebro, N.: Loss Functions for Preference Levels : Regression with Discrete Ordered Labels, in: Proceedings of  
881 the IJCAI multidisciplinary workshop on advances in preference handling, Volume 1, 180–186, AAAI Press, Menlo Park, CA,  
882 2005.  
883

884 Ronneberger, O., Fischer, P., and Brox, T.: U-Net: Convolutional Networks for Biomedical Image Segmentation, in: Navab, N.,  
885 Hornegger, J., Wells, W., Frangi, A. (eds) *Medical Image Computing and Computer-Assisted Intervention (MICCAI 2015)*,  
886 *Lecture Notes in Computer Science*, Volume 9351, Springer, Cham., [https://doi.org/10.1007/978-3-319-24574-4\\_28](https://doi.org/10.1007/978-3-319-24574-4_28), 2015.  
887

888 Sassen, K., Wang, Z., and Liu, D.: Global distribution of cirrus clouds from CloudSat/Cloud-Aerosol Lidar and Infrared  
889 Pathfinder Satellite Observations (CALIPSO) measurements, *J. Geophys. Res.*, Volume 113, D00A12,  
890 <https://doi.org/10.1029/2008JD009972>, 2008.  
891

892 Shi, X., Cao, W., and Raschka, S.: Deep Neural Networks for Rank-Consistent Ordinal Regression Based On Conditional  
893 Probabilities, *Pattern Analysis and Applications*, Volume 26, 941–955, <https://doi.org/10.1007/s10044-023-01181-9>, 2023.  
894

895 Silva, W., Pinto, J. R., and Cardoso, J. S.: A Uniform Performance Index for Ordinal Classification with Imbalanced Classes,  
896 2018 International Joint Conference on Neural Networks (IJCNN), Rio de Janeiro, Brazil, 1-8,  
897 <https://doi.org/10.1109/IJCNN.2018.8489327>, 2018.  
898

899 Simonyan, K., and Zisserman, A.: Very Deep Convolutional Networks for Large-Scale Image Recognition, 3rd International  
900 Conference on Learning Representations (ICLR), Computational and Biological Learning Society, 1-14,  
901 <https://arxiv.org/abs/1409.1556>, 2015.  
902

903 Stephens, G. L., Vane, D. G., Tanelli, S., Im, E., Durden, S., Rokey, M., Reinke, D., Partain, P., Mace, G. G., Austin, R.,  
904 L'Ecuyer, T., Haynes, J., Lebsock, M., Suzuki, K., Waliser, D., Wu, D., Kay, J., Gettelman, A., Wang, Z., and Marchand, R.:  
905 CloudSat mission: Performance and early science after the first year of operation, *J. Geophys. Res.*, Volume 113, D00A18,  
906 <http://doi.org/10.1029/2008JD009982>, 2008.  
907

908 Tanelli, S., Durden, S. L., Im, E., Pak, K. S., Reinke, D. G., Partain, P., Haynes, J. M., and Marchand, R. T.: CloudSat's Cloud  
909 Profiling Radar After Two Years in Orbit: Performance, Calibration, and Processing, *IEEE Trans. Geosci. Remote Sens.*, Volume  
910 46, 3560–3573, <https://doi.org/10.1109/TGRS.2008.2002030>, 2008.  
911

912 TorchVision maintainers and contributors: TorchVision: PyTorch's Computer Vision library, GitHub repository,  
913 <https://github.com/pytorch/vision>, 2016.  
914

915 Trenberth, K. E., Fasullo, J. T., and Kiehl, J.: Earth's global energy budget, *Bulletin of the American Meteorological Society*,  
916 Volume 90, 311–324, <http://doi.org/10.1175/2008BAMS2634.1>, 2009.  
917

918 Watson-Parris, D., Rao, Y., Olivié, D., Seland, Ø., Nowack, P., Camps-Valls, G., Stier, P., Bouabid, S., Dewey, M., Fons, E.,  
919 Gonzalez, J., Harder, P., Jeggle, K., Lenhardt, J., Manshausen, P., Novitasari, M., Ricard, L., and Roesch, C.: ClimateBench v1.0:  
920 A benchmark for data-driven climate projections, *Journal of Advances in Modeling Earth Systems*, Volume 14, Issue 10,  
921 <https://doi.org/10.1029/2021MS002954>, 2022.  
922

923 Winship, C., and Mare, R. D.: Regression Models with Ordinal Variables, *American Sociological Review*, Volume 49, Number 4,  
924 512–525, <https://doi.org/10.2307/2095465>, 1984.

925

926 WMO: Manual on Codes (WMO-No. 306), Volume I.1, Part A, Alphanumeric codes, Code table 1600,  
927 <https://library.wmo.int/idurl/4/35713>, 2019.

928

929 Zantedeschi, V., Falasca, F., Douglas, A., Strange, R., Kusner, M. J., and Watson-Parris, D.: Cumulo: A Dataset for Learning  
930 Cloud Classes, Tackling Climate Change with Machine Learning Workshop, 33rd Conference on Neural Information Processing  
931 Systems (NeurIPS 2019), Vancouver, Canada, <https://doi.org/10.48550/arXiv.1911.04227>, 2019.

932

933 Zeiler, M. D. , Krishnan, D., Taylor, G. W., and Fergus, R. : Deconvolutional networks, in: Proceedings of the 2010 IEEE  
934 Computer Society Conference on Computer Vision and Pattern Recognition (CVPR), San Francisco, CA, USA, 2528-2535,  
935 <https://doi.org/10.1109/CVPR.2010.5539957>, 2010.